Tuning the Morphology and Electronic Properties of Single-Crystal $LiNi_{0.5}Mn_{1.5}O_{4-\delta}$

Stephanie Leigh Spence

Thesis submitted to the faculty of the Virginia Polytechnic Institute and State University in partial fulfillment of the requirements for the degree of

Master of Science
In
Chemistry

Feng Lin, Chair
John R. Morris
Amanda Morris
Ayman M. Karim

October 13th, 2020
Blacksburg, VA

Keywords: Intercalation chemistry, crystal and electronic structures, transition metal oxides, heterogeneous catalysis, support interactions

Tuning the Morphology and Electronic Properties of Single-Crystal $LiNi_{0.5}Mn_{1.5}O_{4-\delta}$

Stephanie Leigh Spence

Academic Abstract

The commercialization of lithium-ion batteries has played a pivotal role in the development of consumer electronics and electric vehicles. In recent years, much research has focused on the development and modification of the active materials of electrodes to obtain higher energies for a broader range of applications. High voltage spinel materials including $LiNi_{0.5}Mn_{1.5}O_{4-\delta}$ (LNMO) have been considered as promising cathode materials to address the increasing demands for improved battery performance due to their high operating potential, high energy density, and stable cycling lifetimes. In an effort to elucidate fundamental structure-property relationships, this thesis explores the tunable properties of single-crystal LNMO. Utilizing facile molten salt synthesis methods, the structural and electronic properties of LNMO can be well controlled. Chapter 2 of this thesis focuses on uncovering the effect of molten salt synthesis parameters including molten salt composition and synthetic temperature on the materials properties. A range of imaging, microscopic, and spectroscopic techniques are used to characterize structural and electronic properties which are investigated in tandem with electrochemical performance. Results indicate the Mn oxidation state is highly dependent on synthesis temperature and can dictate performance, while the molten salt composition strongly influences the particle morphology. In Chapter 3, we explore the concept of utilizing LNMO as a tunable support for heterogeneous metal nanocatalysts, where alteration of the support structure and electronics can have an influence on catalytic properties due to unique support effects. Ultimately, this work illustrates the tunable nature of single-crystal LNMO and can inform the rational design of LNMO materials for energy applications.

Tuning the Morphology and Electronic Properties of Single-Crystal $LiNi_{0.5}Mn_{1.5}O_{4-\delta}$

Stephanie Leigh Spence

General Audience Abstract

The development of lithium-ion batteries has been fundamental to the expansion and prevalence of consumer electronics and electric vehicles in the twenty-first century. Despite their ubiquity, there is an ongoing drive by researchers to address the limitations and improve the quality and performance of lithium ion batteries. Much research has focused on altering the composition, structure, or properties of electrodes at the materials level to design higher achieving batteries. A fundamental understanding of how composition and structure effect battery performance is necessary to progress toward better materials. This thesis focuses on investigating the properties of $LiNi_{0.5}Mn_{1.5}O_{4-\delta}$ (LNMO). LNMO material is considered a promising cathode material to meet the increasing consumer demands for improved battery performance. Through the synthesis methods, the shape of individual particles and the global electronic properties of LNMO can be tuned. In this work, specific synthesis parameters are systematically tuned and the properties of the resultant LNMO materials are explored. Electrochemical testing also evaluates the performance of the materials and offers insights into how they may fair in real battery systems. In an effort to potentially recycle spent battery materials, LNMO is also utilized as a catalyst support. Alteration of shape and electronic properties of the LNMO support can influence the catalytic properties, or the ability of the material to enhance the rate of a chemical reaction. Overall, this thesis explores how LNMO can be tuned and utilized for different applications. This work provides insights for understanding LNMO properties and direction for the development of future battery materials.

Acknowledgements

First and foremost, I would like to thank my advisor Dr. Feng Lin. Thank you for your continued guidance and support. Your advice, insights, and encouragement continuously push me to become a better scientist. Thank you Dr. John Morris, Dr. Amanda Morris, and Dr. Ayman Karim for serving on my committee and for your valuable feedback and suggestions. Thank you to the members of The Lin Lab for guidance, collaboration, support, and friendships that have been vital to my research efforts. I am also grateful for the support and encouragement of all my friends. Finally, thank you to my parents and brothers for their unwavering encouragement and moral support.

Table of Contents

Attributions

The second chapter of this work has been published in *Inorganic Chemistry*, **DOI:** 10.1021/acs.inorgchem.0c01042, and reprinted with permission from the American Chemical Society: Spence, S. L.; Xu, Z.; Sainio, S.; Nordlund, D.; Lin, F. Tuning the Morphology and Electronic Properties of Single-Crystal $LiNi_{0.5}Mn_{1.5}O_{4-\delta}$: Exploring the Influence of LiCl–KCl Molten Salt Flux Composition and Synthesis Temperature. *Inorg. Chem.* **2020**, *59*, 10591–10603. Copyright 2020. It has been formatted for this thesis. Dr. Feng Lin oversaw the project. Zhengrui Xu and Muhammad Mominur Rahman collected SEM images. Dr. Sami Sainio and Dr. Dennis Nordlund collected soft XAS data at SLAC National Acceleration Laboratory. All additional synthesis, experimentation, and analysis were conducted by Stephanie L. Spence.

The third chapter of this work was conceptualized by Dr. Feng Lin and Stephanie L. Spence. Dr. Feng Lin oversaw the project. Muhammad Mominur Rahman collected SEM images. Muhammad Mominur Rahman and Chunguang Kuai collected synchrotron XRD patterns at SLAC National Acceleration Laboratory. Dr. Sami Sainio and Dr. Dennis Nordlund collected soft XAS data at SLAC National Acceleration Laboratory. Crystal K. Waters helped develop the p-nitrophenol reduction experiments. All additional synthesis, experimentation, and analysis were conducted by Stephanie L. Spence.

In the fourth chapter of this work, Dr. Linqin Mu collected the TXM images at SLAC National Acceleration Laboratory. Stephanie L. Spence prepared samples and performed data analysis.

Abbreviations

FY, Fluorescence yield

HOMO, Highest occupied molecular orbital

LCO, $LiCoO_2$

LIB, Lithium-ion battery

LNMO, $LiNi_{0.5}Mn_{1.5}O_4$

NMC, $Li(Ni_{1-x-y}Mn_xCo_y)O_2$

SEI, Solid-electrolyte interphase

SEM, Scanning electron microscopy

TEY, Total electron yield

TM, Transition metal

TMO, Transition metal oxide

TXM, Transmission X-ray microscopy

UV-VIS, Ultraviolet-visible spectroscopy

XAS, X-ray absorption spectroscopy

XRD, X-ray diffraction

Chapter 1. Introduction

1.1. Spinel Transition Metal Oxides

Transition metal oxide materials have been vital to the development of batteries into ubiquitous consumer products. The first commercialized lithium-ion batteries (LIBs) were developed in the early 1990s and used $LiCoO_2$ (LCO) as cathode materials.[1] Doping LCO with Ni and Mn has led to a new class of $Li(Ni_{1-x-y}Mn_xCo_y)O_2$ (NMC) materials. NMC layered materials are attractive because they are cheaper, safer, and more environmentally friendly than just Co containing materials, especially as research moves its focus toward more Ni-rich, Co-poor materials. Both LCO and NMC have layered crystal structures where transition metals, oxygen, and lithium form alternating layers. Upon charging and discharging, Li ions migrate from and are intercalated into the lattice of the cathode through the two-dimensional Li layers.[2] Layered materials are the most commonly used cathodes for commercial LIBs, however, these materials are limited by capacity fading, instability during high-voltage operation leading to irreversible oxygen and Li loss and electrolyte side reactions, as well as structural or chemical rearrangements occurring during operation. This rearrangement leads to surface reconstruction which hinders performance and lifetime.[3]

As demands for higher energy density, power density, cycle-life, and safety in consumer batteries increases, high-voltage spinel materials offer potential solutions.[4] Spinel $LiMn_2O_4$ is an alternative to layered material due to its low cost, low toxicity, high rate capability, abundance of raw materials, and three-dimensional framework which allows for fast Li intercalation.[5] The Ni substituted variation $LiNi_xMn_{2-x}O_4$, or LNMO, has gained attention due to the improved cycling stability, higher working potential, and greater energy versus pure phase $LiMn_2O_4$.[6] Furthermore, substitution of Mn by Ni in LNMO stabilizes the average Mn oxidation at 4+, so Ni becomes the

only redox active metal which improves electrochemical performance.[7] LNMO has a high working potential (4.7-4.9 V vs Li/Li^+), a theoretical capacity of 148 mAh/g, a high energy density of 650 Wh/kg, and three-dimensional Li diffusion paths leading to high rate capability.[4,6,8] Single-crystal LNMO particles can be easily obtained with various synthesis methods. Single-crystal materials offer high chemomechanical stability, making them uniquely suited to develop high performance battery materials and ideal for continued study.[9]

This thesis focuses on tuning the morphological and electronic properties of single-crystal spinel LNMO for battery cathode and catalysis support applications. This chapter discusses the relevant background of spinel LNMO including its crystal and electronic structures, practical challenges and possible solutions, as well as the advantages of the molten salt synthesis to create single-crystal materials and tune LNMO materials parameters for use as battery cathodes or catalyst supports.

1.2. Two Crystallographic Forms of Spinel $LiNi_{0.5}Mn_{1.5}O_4$

Spinel LNMO adopts two crystallographic structures: an ordered primitive simple cubic of the $P4_332$ space group with Mn and Ni ions occupying two separate octahedral sites, or a disordered face centered cubic spinel of the $Fd\bar{3}m$ space group where Mn and Ni ions are in a random arrangement in the octahedral sites.[10] In the disordered material, oxygen forms a cubic close packed structure with Ni and Mn randomly arranged on the 16d octahedral sites, oxygen on the 8a tetrahedral sites, and lithium occupying the 32e sites. In the ordered structure, Ni occupies 4a positions while Mn occupies 12b positions. Oxygen is in the 8c and 24e sites and Li is in 4c sites.[4] While the chemical composition of the two structures is the same, small differences in the

electronic properties of the materials lead to differences in electrochemical performance. **Figure 1-1** illustrates the transition metal arrangement in the crystal structures of the two material phases.

Studies comparing the structural and electronic properties of both phases of LNMO have concluded that the disordered spinel is favored at calcination temperatures above 700 °C due to slow kinetic formation whereas the ordered phase requires annealing below 700°C to form.[10–12] The stoichiometric ordered phase is more theoretically favorable because the higher temperatures used to synthesize the disordered phase leads to oxygen vacancies.[13] However, the presence of oxygen vacancies may also lead to the reduction of a small amount of inactive Mn^{4+} to Mn^{3+} in order to compensate for oxygen loss.[14,15] Rock-salt $Li_xNi_{1-x}O$-type impurities may also occur during high temperature synthesis accompanying the formation of the disordered phase. Development of this Li-containing rock salt phase can also increase the Mn/Ni ratio in the disordered spinel phase, increasing the Mn^{3+} without the formation of oxygen vacancies.[16] This redox-active Mn^{3+} in the disordered phase slightly improves electronic conductivity and Li^+ diffusion and is responsible for enhanced electrochemical behavior. In contrast, the $P4_332$ phase contains Ni^{2+} and Mn^{4+} fixed oxidation states where Ni has been found to be the only redox-active transition metal.[17]

Ordered $P4_332$ phase material can be obtained from disordered $Fd\bar{3}m$ phase by post synthesis annealing near 700 °C followed by a slow cooling in order to promote re-ordering of cations. Cation disorder is closely linked to the presence of Mn^{3+}, therefore, research on LNMO crystal structures suggests that careful control of synthetic parameters can influence both Ni and Mn ordering and the electronic structure of LNMO materials.[18,19] It should be noted that practically, pure phase disordered or ordered phases of LNMO are difficult to obtain and varying degrees of ordering/disordering are likely present throughout local regions of LNMO particles.[16]

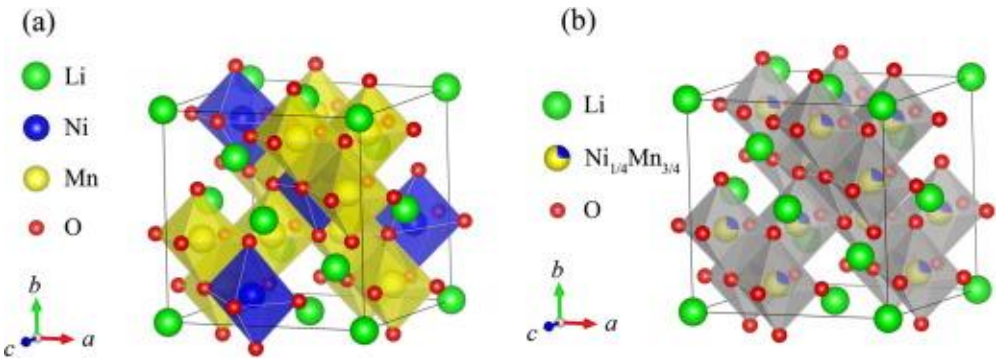

Figure 1-1. Crystal structure of (a) ordered ($P4_332$) and (b) disordered ($Fd\bar{3}m$) LNMO. Reprinted with permission from Elsevier: Chen, Y.; Sun, Y.; Huang, X. Origin of the Ni/Mn Ordering in High-Voltage Spinel $LiNi_{0.5}Mn_{1.5}O_4$: The Role of Oxygen Vacancies and Cation Doping. *Comput. Mater. Sci.* **2016**, *115*, 109–116.[13] Copyright 2016.

The existence of two structures for LNMO leads to differences in materials characteristics and electrochemical performance. An increase in disordering has been found to increase ionic transport kinetics.[20] The presence of Mn^{3+} in the disordered material is also believed to improve the rate performance of the material during electrochemical cycling due to improved electronic conductivity and Li^+ diffusion. In the stoichiometric ordered material, Ni^{2+}/Ni^{3+} and Ni^{3+}/Ni^{4+} redox couples occur as two distinct two-phase regions with negligible voltage differences, and so appear as a single voltage plateau around ~ 4.7 V vs Li/Li^+ in the charge/discharge curve. Mn remains stable in the 4+ oxidation state and does not contribute to the capacity. The electrochemically active Mn^{3+} in the disordered phase material leads to an additional voltage plateau at ~ 4.0 V vs Li/Li^+ as Mn participates in a redox event, which may be desirable for improved cycle life.[16] The disordered phase also leads to increased solid-solution behavior which is represented by two distinct regions with less defined plateaus in the voltage region of Ni redox, compared to the two-phase mechanism which dominates in the ordered phase material.[20] The

typical charge and discharge profiles of the two materials are shown in **Figure 1-2**.[21] Overall, it is suggested that the disordered phase material has better electrochemical performance and structural reversibility at faster rates due to the one-step phase transition.[10] The interrelationship between Mn^{3+} content, the cation ordering, and oxygen vacancies are not simply straightforward. Careful syntheses are needed in order to tune these properties individually and determine how the Mn^{3+} content or the extent of order/disorder may offer enhanced electrochemical performance.

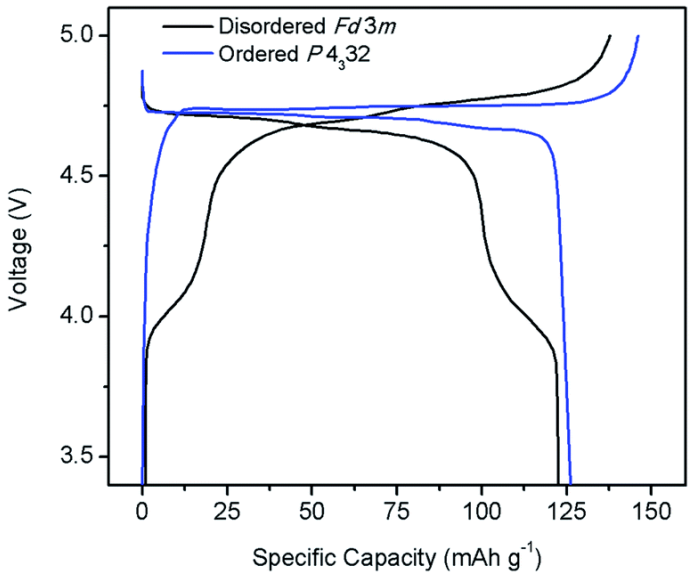

Figure 1-2. Typical charge/discharge profile of ordered $P4_332$ and disordered $Fd\bar{3}m$ LNMO. Reprinted with permission from The Royal Society of Chemistry: Manthiram, A.; Chemelewski, K.; Lee, E. S. A Perspective on the High-Voltage $LiMn_{1.5}Ni_{0.5}O_4$ spinel Cathode for Lithium-Ion Batteries. In *Energy and Environmental Science*; 2014; Vol. 7, pp 1339–1350.[21] Copyright 2014.

1.3. Challenges of LNMO

While spinel LNMO's remain a promising cathode, the material also faces many drawbacks. As mentioned previously, the disordered phase spinel may be desirable for enhanced

electrochemical behaviors, however, the existence of more Mn^{3+} in the disordered structure leads to Jahn Teller distortion of the MnO_6 octahedra which reduces crystal symmetry, as well as transition metal dissolution via the disproportionation reaction ($2Mn^{3+} \rightarrow Mn^{2+} + Mn^{4+}$) which can lead to capacity fading.[7,22] The Mn dissolution has been reported to be the largest barrier of the practical application of LNMOs.[23]

The high voltage necessary for Ni redox also leads to increased side reactions with the electrolyte. **Figure 1-3** depicts the relative energies and densities of states for the redox couples in LNMO. The highest occupied molecular orbital (HOMO) of a typical carbonate electrolyte used with this cathode is around 4.3 V vs Li/Li^+.[22] The spinel will begin to oxidize the electrolyte at this voltage unless a stable solid-electrolyte interphase (SEI) layer is formed on the surface of the active material.[22,24] At ~ 5.0 V vs Li/Li^+, oxygen evolution and electrolyte degradation can occur which leads to severe capacity fading, especially at elevated temperatures. Understanding the intrinsic interfacial challenges of so called "5-V electrodes" is therefore necessary for optimization and commercialization of the materials. Several strategies have been undertaken to mitigate the problems associated with high voltage operation including doping, coating, and rational design of LNMO particles with specific crystal orientations to minimize the severity of side reactions.[25]

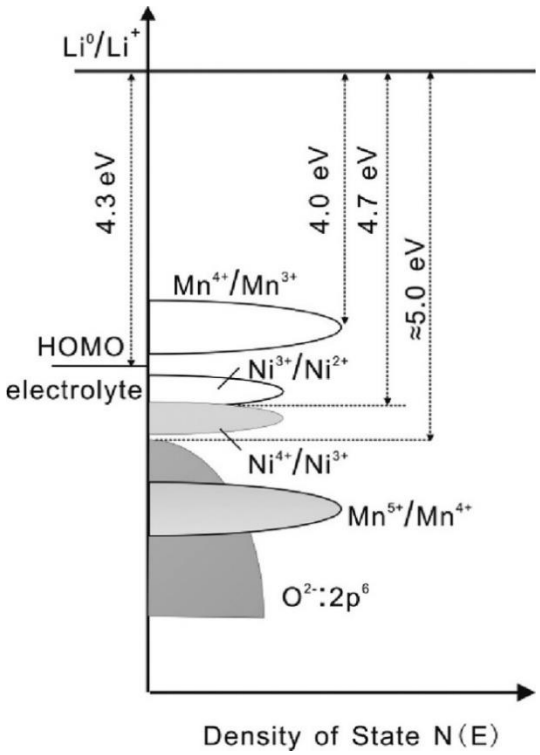

Figure 1-3. Schematic of energy versus density of states for LNMO. Reprinted with permission from American Chemical Society: Song, J.; Shin, D. W.; Lu, Y.; Amos, C. D.; Manthiram, A.; Goodenough, J. B. Role of Oxygen Vacancies on the Performance of $Li[Ni_{0.5-X}Mn_{1.5+x}]O_4$ (x = 0, 0.05, and 0.08) Spinel Cathodes for Lithium-Ion Batteries. *Chem. Mater.* **2012**, *24* (15), 3101–3109.[22] Copyright 2012.

1.4. Microstructure

Both particle size and morphology are vital factors in the development of LNMO into efficient cathode materials. As previously discussed, the high voltage operation required for the material can lead to significant side reactions. Nanometer sized particles with large surface areas, which tend to agglomerate into larger secondary particles, are prone to more interfacial reactions with electrolyte and increased Mn dissolution.[26,27] On the other hand, particles that are several microns in size will have increased Li^+ diffusion lengths, which can worsen electrochemical

performance by leading to decreased specific capacity and energy. In designing LNMO particles of appropriate size, there is an apparent tradeoff to obtain either long cycle life or fast rate performance.[26] Micron sized single-crystal particles are therefore desired to offer both the best stability and electrochemical performance.[26]

In addition to size, morphology has been shown to be influential in the performance of LNMO. Despite the improved kinetics of the disordered phase over the ordered, the specific crystallographic facets a particle possesses may be more influential on electrochemical performance than bulk crystal structure.[26,28] The most thermodynamically stable morphology of LNMO is octahedrons enclosed by (111) facets.[27] This facet has the lowest surface energy and can facilitate the formation of a stable SEI leading to stable cycling performance.[27] However, other crystal orientations may also be desirable for depending on the required applications. For example, studies have reported polyhedral or truncated octahedral structures with exposed (110) facets have led to improved rate capability over octahedrons.[29,30] Careful control of the microstructure and crystal orientations of LNMO is desirable for the rational design of the material.

1.4.1. Controlling Properties of LNMO via Molten Salt Synthesis

The size and shape of metal oxides can be engineered during growth by altering chemical and physical conditions during synthesis.[31] After the initial nucleation of the particles, growth generally favors the crystal facets with faster formation rates or that do not use growth-inhibiting capping agents. Unsaturated corner sites or exposed high-index crystal facets may have different chemical properties or reactivity than saturated sites or low-index crystal facets.[32] Synthesizing facets of high Miller indices is generally more difficult than low indices because they are generally not thermodynamically favorable and tend to have high growth rates.[33] Growth control reagents

can be used to kinetically direct growth to prevent the formation of more favorable facets.[34] Nevertheless, particles with well-controlled kinetic shape and size may evolve under reaction conditions toward thermodynamically favored structures.

LNMO has been synthesized via co-precipitation,[35,36] solid state[37–39], carbon exo-templating,[40] and molten salt methods.[41–43] The molten salt synthesis is of particular interest to our work because it allows for facile control of surface structure. The method uses a low melting point salt or mixture of salts as a reaction medium and can produce high purity powders of a single crystal phase.[41] Particle size and morphology can be tuned by varying TM precursors,[44] molten salts, salt to TM ratios, synthesis temperatures, and synthesis durations. Examining the effect of synthetic variables on LNMO formation showed that average particle size increases with increasing LiCl salt, temperature, and synthetic times.[41,45]

Knowledge of the effects of each synthetic parameter on the resulting morphological structure can help to guide synthetic design. For example, metal oxides with all high energy polar surfaces exposed have been selectively synthesized.[46] The molten salt method was used to synthesize pure phase $Fd\bar{3}m$ LNMO in plate shapes with (112) surface facets and octahedral shapes with (111) facets using a LiCl-KCl flux.[47] Varying the ratio of LiCl and KCl affects the formation of crystal facets based on the melting point of the salt flux, which may change the favorability of each facet. Octahedrons were synthesized using a LiCl-KCl flux at 650 °C, 300 °C above the eutectic melting point, allowing the thermodynamically stable (111) facets to form. The plates were synthesized using LiCl flux at 750 °C, only 140 °C above the melting point of pure LiCl, allowing the more kinetically favorable (112) facets to predominate. In LNMO electrodes, plates containing (112) facets experienced continuous side reactions leading to structural change and TM dissolution, while the denser atomic arrangement and lower surface energy of octahedrons

enclosed by (111) facets made the electrodes less vulnerable to electrolyte oxidation.[48] The corresponding SEM images of the LNMO particles are shown in **Figure 1-4** to illustrate the tunable morphology achieved from the molten salt synthesis.

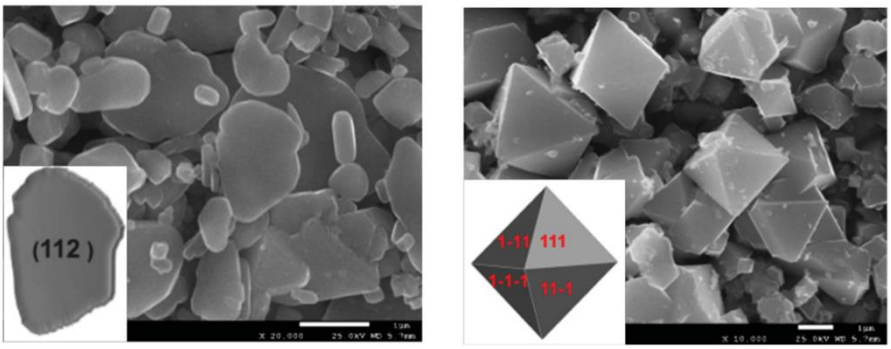

Figure 1-4. SEM images of LNMO plates with exposed (112) facets and octahedrons with exposed (111) facets. Reprinted with permission from The Royal Society of Chemistry: Hai, B.; Shukla, A. K.; Duncan, H.; Chen, G. The Effect of Particle Surface Facets on the Kinetic Properties of $LiMn_{1.5}Ni_{0.5}O_4$ Cathode Materials. *J. Mater. Chem. A* **2013**, *1* (3), 759–769.[47] Copyright 2013.

The advantage of using the molten salt method over the traditional co-precipitation method for metal oxides synthesis is that it provides better control over the particle morphology. Wet synthesis methods also have more complicated synthesis routes and high associated costs. In addition, shape and size control of LNMO with high purity is difficult to achieve due to phase separation and sintering occurring in syntheses with prolonged high temperature calcinations which are needed in the wet-chemistry based methods.[49] The variables in the molten salt method can be easily controlled and tuned in one-step. The molten salt method is also able to obtain pure phase $Fd\bar{3}m$ LNMO with limited impurity phases due to the faster phase formation in the molten media compared to other synthesis methods.[41] The ability of the molten salt synthesis method to

govern the shape, size, and crystal orientation of LNMO allows for rational design of the material to help mitigate the challenges associated with operation in batteries, or to alter materials properties for additional applications, such as for use as catalyst supports.

1.5. LNMO as Catalyst Supports

Supported metal catalysts represent a class of heterogeneous catalysts and are used for chemical upgrading in many research fields including the petrochemical industry, medicine production, environmental protection, and energy technology. A catalytically active metal like nano sized gold, platinum, palladium, or iridium is isolated on a support material and the composite material may exhibit unique support effects that can alter the activity of the catalyst toward certain reactions. The origins of support effects may be structural, electronic, or due to a synergistic effect between the metal and the support, but the origin of the effect has not been fully quantified and all possible effect contributions have not been confidently decoupled.

The ability of Li containing TMO to intercalate and extract Li ions makes them effective for cathode materials for use in Li ion batteries. This feature also makes them attractive as a tunable catalyst supports, since controllably delithiating the material tunes orbital occupancy and TM−O covalency.[50] Furthermore, the lifetime of Li ion batteries is one to three years in digital products and five to eight years in vehicles.[51] Li ion battery waste also contains heavy metals and toxic electrolytes. Utilizing material typically used as battery cathode materials as catalyst supports is an opportunity to potentially repurpose battery materials. The stability of spinel LNMO makes it ideal for studies as tunable catalyst supports. Through delithiation, the oxidation state of TMs can be tuned, influencing of the number of TM-3d electrons and, ultimately, catalytic activity.[52]

Spinel materials typically have low catalytic activity for water oxidation, but, upon Li removal, spinel $LiMn_2O_4$ formed a unique open structure active for water oxidation.[53] Catalytic active sites are also dependent on the degree of delithiation.[54] Li containing layered and spinel TMO have been found to be active for the oxygen evolution reaction, an intensive 4 electron process, as a result of Li mobility.[50,53] Combining both structural and electronic control of LNMO obtained through the molten salt synthesis method, we can develop a catalogue of continuously tunable support materials. This study will provide a new opportunity to examine each of the many parameters affecting support interactions in isolation as well as provide an opportunity to potentially repurpose spent cathode materials. Understanding and optimizing support effects can inform the design of novel catalyst materials for selective chemical upgrading.

1.6. Research Goals

The Li intercalation properties of TMOs make them effective for battery cathode materials, with spinel material offering high structural stability and energy density to potentially meet increasing consumer demands. In addition, the tunable properties of Li-TMO, particularly single-crystal LNMO, allow these materials to be rationally altered for use at catalyst supports. This thesis explores how properties of spinel LNMO can be tuned via a molten salt synthesis method. Chapter 2 focuses on exploring the synthetic parameters of the molten salt synthesis to influence materials properties including crystal structure, electronic structure, and morphology, as well as examining the effect of these properties on the electrochemical performance of the resultant materials in battery cells. Chapter 3 will present an alternative application for single-crystal, faceted LNMO as tunable supports for noble metal nanocatalysts. Chapter 4 will summarize the work and provide research perspectives. Ultimately, this work strives to illustrate that the molten salt synthesis

method works as a toolbox allowing for systematic control the properties of LNMO or other TMOs. With a continuously tunable system, we are able to study and optimize individual parameters of LNMO for various applications.

1.7. References

(1) Pimenta, V.; Sathiya, M.; Batuk, D.; Abakumov, A. M.; Giaume, D.; Cassaignon, S.; Larcher, D.; Tarascon, J. M. Synthesis of Li-Rich NMC: A Comprehensive Study. *Chem. Mater.* **2017**, *29* (23), 9923–9936.

(2) Whittingham, M. S. Lithium Batteries and Cathode Materials. *Chem. Rev.* **2004**, *104* (10), 4271–4301.

(3) Lin, F.; Markus, I. M.; Nordlund, D.; Weng, T. C.; Asta, M. D.; Xin, H. L.; Doeff, M. M. Surface Reconstruction and Chemical Evolution of Stoichiometric Layered Cathode Materials for Lithium-Ion Batteries. *Nat. Commun.* **2014**, *5*, 3529.

(4) Santhanam, R.; Rambabu, B. Research Progress in High Voltage Spinel $LiNi_{0.5}Mn_{1.5}O_4$ Material. *J. Power Sources* **2010**, *195* (17), 5442–5451.

(5) Thackeray, M. M.; David, W. I. F.; Bruce, P. G.; Goodenough, J. B. Lithium Insertion into Manganese Spinels. *Mater. Res. Bull.* **1983**, *18* (4), 461–472.

(6) Zhong, Q. Synthesis and Electrochemistry of $LiNi_xMn_{2-x}O_4$. *J. Electrochem. Soc.* **1997**, *144* (1), 205.

(7) Rana, J.; Glatthaar, S.; Gesswein, H.; Sharma, N.; Binder, J. R.; Chernikov, R.; Schumacher, G.; Banhart, J. Local Structural Changes in $LiMn_{1.5}Ni_{0.5}O_4$ Spinel Cathode Material for Lithium-Ion Batteries. *J. Power Sources* **2014**, *255*, 439–449.

(8) Patoux, S.; Daniel, L.; Bourbon, C.; Lignier, H.; Pagano, C.; Le Cras, F.; Jouanneau, S.; Martinet, S. High Voltage Spinel Oxides for Li-Ion Batteries: From the Material Research to the Application. *J. Power Sources* **2009**, *189* (1), 344–352.

(9) Li, J.; Cameron, A. R.; Li, H.; Glazier, S.; Xiong, D.; Chatzidakis, M.; Allen, J.; Botton, G. A.; Dahn, J. R. Comparison of Single Crystal and Polycrystalline $LiNi_{0.5}Mn_{0.3}Co_{0.2}O_2$

Positive Electrode Materials for High Voltage Li-Ion Cells. J. Electrochem. Soc. 2017, 164 (7), A1534–A1544.

(10) Kim, J. H.; Myung, S. T.; Yoon, C. S.; Kang, S. G.; Sun, Y. K. Comparative Study of $LiNi_{0.5}Mn_{1.5}O_{4-\delta}$ and $LiNi_{0.5}Mn_{1.5}O_4$ Cathodes Having Two Crystallographic Structures: Fd3m and $P4_332$. *Chem. Mater.* **2004**, *16* (5), 906–914.

(11) Kim, S.; Hegde, V. I.; Yao, Z.; Lu, Z.; Amsler, M.; He, J.; Hao, S.; Croy, J. R.; Lee, E.; Thackeray, M. M.; Wolverton, C. First-Principles Study of Lithium Cobalt Spinel Oxides: Correlating Structure and Electrochemistry. *ACS Appl. Mater. Interfaces* **2018**, *10* (16), 13479–13490.

(12) Greco, G.; Brutti, S.; Vitucci, F. M.; Lombardo, L.; Köntje, M.; Savoini, A.; Paolone, A.; Panero, S. Investigation of the Chemical Disorder of $LiNi_{0.5}Mn_{1.5}O_4$ Lattice by Means of Extended X-Ray Absorption Fine Structure Spectroscopy. *J. Phys. Chem. C* **2014**, *118* (46), 26471–26478.

(13) Chen, Y.; Sun, Y.; Huang, X. Origin of the Ni/Mn Ordering in High-Voltage Spinel $LiNi_{0.5}Mn_{1.5}O_4$: The Role of Oxygen Vacancies and Cation Doping. *Comput. Mater. Sci.* **2016**, *115*, 109–116.

(14) Jafta, C. J.; Mathe, M. K.; Manyala, N.; Roos, W. D.; Ozoemena, K. I. Microwave-Assisted Synthesis of High-Voltage Nanostructured $LiMn_{1.5}Ni_{0.5}O_4$ Spinel: Tuning the Mn^{3+} Content and Electrochemical Performance. *ACS Appl. Mater. Interfaces* **2013**, *5* (15), 7592–7598.

(15) Kunduraci, M.; Al-Sharab, J. F.; Amatucci, G. G. High-Power Nanostructured $LiMn_{2-X}Ni_XO_4$ High-Voltage Lithium-Ion Battery Electrode Materials: Electrochemical Impact of Electronic Conductivity and Morphology. *Chem. Mater.* **2006**, *18* (15), 3585–3592.

(16) Aktekin, B.; Valvo, M.; Smith, R. I.; Sørby, M. H.; Lodi Marzano, F.; Zipprich, W.; Brandell, D.; Edström, K.; Brant, W. R. Cation Ordering and Oxygen Release in $LiNi_{0.5-x}Mn_{1.5+x}O_{4-y}$ (LNMO): In Situ Neutron Diffraction and Performance in Li Ion Full Cells. *ACS Appl. Energy Mater.* **2019**, *2* (5), 3323–3335.

(17) Kan, W. H.; Kuppan, S.; Cheng, L.; Doeff, M.; Nanda, J.; Huq, A.; Chen, G. Crystal Chemistry and Electrochemistry of $Li_xMn_{1.5}Ni_{0.5}O_4$ Solid Solution Cathode Materials. *Chem. Mater.* **2017**, *29* (16), 6818–6828.

(18) Moorhead-Rosenberg, Z.; Shin, D. W.; Chemelewski, K. R.; Goodenough, J. B.; Manthiram, A. Quantitative Determination of Mn^{3+} Content in $LiMn_{1.5}Ni_{0.5}O_4$ Spinel Cathodes by Magnetic Measurements. *Appl. Phys. Lett.* **2012**, *100* (21).

(19) Amdouni, N.; Zaghib, K.; Gendron, F.; Mauger, A.; Julien, C. M. Structure and Insertion Properties of Disordered and Ordered $LiNi_{0.5}Mn_{1.5}O_4$ Spinels Prepared by Wet Chemistry. *Ionics (Kiel).* **2006**, *12* (2), 117–126.

(20) Duncan, H.; Hai, B.; Leskes, M.; Grey, C. P.; Chen, G. Relationships between Mn^{3+} Content, Structural Ordering, Phase Transformation, and Kinetic Properties in $LiNi_xMn_{2-x}O_4$ Cathode Materials. *Chem. Mater.* **2014**, *26* (18), 5374–5382.

(21) Manthiram, A.; Chemelewski, K.; Lee, E. S. A Perspective on the High-Voltage $LiMn_{1.5}Ni_{0.5}O_4$ spinel Cathode for Lithium-Ion Batteries. In *Energy and Environmental Science*; 2014; Vol. 7, pp 1339–1350.

(22) Song, J.; Shin, D. W.; Lu, Y.; Amos, C. D.; Manthiram, A.; Goodenough, J. B. Role of Oxygen Vacancies on the Performance of $Li[Ni_{0.5-X}Mn_{1.5+x}]O_4$ (x = 0, 0.05, and 0.08) Spinel Cathodes for Lithium-Ion Batteries. *Chem. Mater.* **2012**, *24* (15), 3101–3109.

(23) Kim, J. H.; Pieczonka, N. P. W.; Yang, L. Challenges and Approaches for High-Voltage

Spinel Lithium-Ion Batteries. *ChemPhysChem*. July 21, 2014, pp 1940–1954.

(24) Julien, C. M.; Mauger, A. Review of 5-V Electrodes for Li-Ion Batteries: Status and Trends. *Ionics (Kiel).* **2013**, *19* (7), 951–988.

(25) Ma, J.; Hu, P.; Cui, G.; Chen, L. Surface and Interface Issues in Spinel $LiNi_{0.5}Mn_{1.5}O_4$: Insights into a Potential Cathode Material for High Energy Density Lithium Ion Batteries. *Chem. Mater.* **2016**, *28* (11), 3578–3606.

(26) Cabana, J.; Zheng, H.; Shukla, A. K.; Kim, C.; Battaglia, V. S.; Kunduraci, M. Comparison of the Performance of $LiNi_{1/2}Mn_{3/2}O_4$ with Different Microstructures. *J. Electrochem. Soc.* **2011**, *158* (9), A997.

(27) Lin, H. B.; Zhang, Y. M.; Rong, H. B.; Mai, S. W.; Hu, J. N.; Liao, Y. H.; Xing, L. D.; Xu, M. Q.; Li, X. P.; Li, W. S. Crystallographic Facet- and Size-Controllable Synthesis of Spinel $LiNi_{0.5}Mn_{1.5}O_4$ with Excellent Cyclic Stability as Cathode of High Voltage Lithium Ion Battery. *J. Mater. Chem. A* **2014**, *2* (30), 11987–11995.

(28) Chemelewski, K. R.; Lee, E. S.; Li, W.; Manthiram, A. Factors Influencing the Electrochemical Properties of High-Voltage Spinel Cathodes: Relative Impact of Morphology and Cation Ordering. *Chem. Mater.* **2013**, *25* (14), 2890–2897.

(29) Chen, Z.; Zhao, R.; Du, P.; Hu, H.; Wang, T.; Zhu, L.; Chen, H. Polyhedral $LiNi_{0.5}Mn_{1.5}O_4$ with Excellent Electrochemical Properties for Lithium-Ion Batteries. *J. Mater. Chem. A* **2014**, *2* (32), 12835–12848.

(30) Liu, H.; Zhang, X.; He, X.; Senyshyn, A.; Wilken, A.; Zhou, D.; Fromm, O.; Niehoff, P.; Yan, B.; Li, J.; Muehlbauer, M.; Wang, J.; Schumacher, G.; Paillard, E.; Winter, M.; Li, J. Truncated Octahedral High-Voltage Spinel $LiNi_{0.5}Mn_{1.5}O_4$ Cathode Materials for Lithium Ion Batteries: Positive Influences of Ni/Mn Disordering and Oxygen Vacancies. *J.*

Electrochem. Soc. **2018**, *165* (9), A1886–A1896.

(31) Wang, Y.; Liu, H.; Bao, M.; Li, B.; Su, H.; Wen, Y.; Wang, F. Structural-Controlled Synthesis of Manganese Oxide Nanostructures and Their Electrochemical Properties. *J. Alloys Compd.* **2011**, *509* (33), 8306–8312.

(32) Liu, L.; Corma, A. Metal Catalysts for Heterogeneous Catalysis: From Single Atoms to Nanoclusters and Nanoparticles. *Chem. Rev.* **2018**, *118* (10), 4981–5079.

(33) Cuenya, B. R.; Behafarid, F. Nanocatalysis Size- and Shape-Dependent Chemisorption and Catalytic Reactivity. *Surf. Sci. Rep.* **2015**, *70*, 135–187.

(34) Linic, S.; Christopher, P.; Xin, H.; Marimuthu, A. Catalytic and Photocatalytic Transformations on Metal Nanoparticles with Targeted Geometric and Plasmonic Properties. *Acc. Chem. Res.* **2013**, *46* (8), 1890–1899.

(35) Fan, Y.; Wang, J.; Ye, X.; Zhang, J. Physical Properties and Electrochemical Performance of $LiNi_{0.5}Mn_{1.5}O_4$ Cathode Material Prepared by a Coprecipitation Method. *Mater. Chem. Phys.* **2007**, *103*, 19–23.

(36) Zhang, M.; Liu, Y.; Xia, Y.; Qiu, B.; Wang, J.; Liu, Z. Simplified Co-Precipitation Synthesis of Spinel $LiNi_{0.5}Mn_{1.5}O_4$ with Improved Physical and Electrochemical Performance. *J. Alloys Compd.* **2014**, *598*, 73–78.

(37) Fang, H.; Wang, Z.; Li, X.; Guo, H.; Peng, W. Low Temperature Synthesis of $LiNi_{0.5}Mn_{1.5}O_4$ Spinel. *Mater. Lett.* **2006**, *60* (9–10), 1273–1275.

(38) Xiang, Y.; Yin, Z.; Zhang, Y.; Li, X. Effects of Synthesis Conditions on the Structural and Electrochemical Properties of the Li-Rich Material $Li[Li_{0.2}Ni_{0.17}Co_{0.16}Mn_{0.47}]O_2$ via the Solid-State Method. *Electrochim. Acta* **2013**, *91*, 214–218.

(39) Jiao, C.; Wang, L.; Zuo, Y.; Ni, P.; Liang, G. Solid-State Synthesis of Spherical

Hierarchical $LiNi_{0.5}Mn_{1.5}O_4$ through an Improved Calcination Method and Its Cyclic Performance for 5 V Lithium Ion Batteries. *Solid State Ionics* **2015**, *277*, 50–56.

(40) Raja, M. W.; Mahanty, S.; Basu, R. N. Multi-Faceted Highly Crystalline $LiMn_2O_4$ and $LiNi_{0.5}Mn_{1.5}O_4$ Cathodes Synthesized by a Novel Carbon Exo-Templating Method. *Solid State Ionics* **2009**, *180* (23–25), 1261–1266.

(41) Kim, J. H.; Myung, S. T.; Sun, Y. K. Molten Salt Synthesis of $LiNi_{0.5}Mn_{1.5}O_4$ Spinel for 5 V Class Cathode Material of Li-Ion Secondary Battery. *Electrochim. Acta* **2004**, *49* (2), 219–227.

(42) Wen, L.; Lu, Q.; Xu, G. Molten Salt Synthesis of Spherical $LiNi_{0.5}Mn_{1.5}O_4$ Cathode Materials. *Electrochim. Acta* **2006**, *51* (21), 4388–4392.

(43) Kim, J. H.; Kang, Y. C. Electrochemical Properties of Nanosized $Li_2MnO_3 \cdot Li(Ni_{0.8}Co_{0.15}Al_{0.05})O_2$ Composite Cathode Powders. *Int. J. Electrochem. Sci.* **2013**, *8* (3), 3664–3675.

(44) Li, C.; Liu, Z.; Zhou, H.; Haminhngoc; Zhu, F.; Guo, Q.; Zhao*, Z. Molten Salt Synthesis of $SrTiO_3$ Using TiO_2 with Different Morphology as a Precursor. *Integr. Ferroelectr.* **2015**, *162* (1), 113–121.

(45) Li, S.; Xie, J.; Zhao, D.; Geng, S.; Li, H.; Li, C.; Cui, X.; Zhang, N. Morphological Evolution of Spinel Disordered $LiNi_{0.5}Mn_{1.5}O_4$ Cathode Materials for Lithium-Ion Batteries by Modified Solid-State Method. *Ionics (Kiel).* **2019**, *25* (5), 1999–2006.

(46) Xu, T.; Zhou, X.; Jiang, Z.; Kuang, Q.; Xie, Z.; Zheng, L. Syntheses of Nano/Submicrostructured Metal Oxides with All Polar Surfaces Exposed via a Molten Salt Route. *Cryst. Growth Des.* **2009**, *9* (1), 192–196.

(47) Hai, B.; Shukla, A. K.; Duncan, H.; Chen, G. The Effect of Particle Surface Facets on the

Kinetic Properties of $LiMn_{1.5}Ni_{0.5}O_4$ Cathode Materials. *J. Mater. Chem. A* **2013**, *1* (3), 759–769.

(48) Kuppan, S.; Duncan, H.; Chen, G. Controlling Side Reactions and Self-Discharge in High-Voltage Spinel Cathodes: The Critical Role of Surface Crystallographic Facets. *Phys. Chem. Chem. Phys.* **2015**, *17* (39), 26471–26481.

(49) Cai, Y.; Huang, S. Z.; She, F. S.; Liu, J.; Zhang, R. L.; Huang, Z. H.; Wang, F. Y.; Wang, H. E. Facile Synthesis of Well-Shaped Spinel $LiNi_{0.5}Mn_{1.5}O_4$ Nanoparticles as Cathode Materials for Lithium Ion Batteries. *RSC Adv.* **2016**, *6* (4), 2785–2792.

(50) Lu, Z.; Wang, H.; Kong, D.; Yan, K.; Hsu, P.-C.; Zheng, G.; Yao, H.; Liang, Z.; Sun, X.; Cui, Y. Electrochemical Tuning of Layered Lithium Transition Metal Oxides for Improvement of Oxygen Evolution Reaction. *Nat. Commun.* **2014**, *5* (1), 4345.

(51) Zheng, X.; Zhu, Z.; Lin, X.; Zhang, Y.; He, Y.; Cao, H.; Sun, Z. A Mini-Review on Metal Recycling from Spent Lithium Ion Batteries. *Engineering* **2018**, *4* (3), 361–370.

(52) Okubo, M.; Yamada, A. Molecular Orbital Principles of Oxygen-Redox Battery Electrodes. *ACS Appl. Mater. Interfaces* **2017**, *9* (42), 36463–36472.

(53) Robinson, D. M.; Go, Y. B.; Greenblatt, M.; Dismukes, G. C. Water Oxidation by λ-MnO_2: Catalysis by the Cubical Mn_4O_4 Subcluster Obtained by Delithiation of Spinel LiMn2O4. *J. Am. Chem. Soc.* **2010**, *132* (33), 11467–11469.

(54) Lu, Z.; Chen, G.; Li, Y.; Wang, H.; Xie, J.; Liao, L.; Liu, C.; Liu, Y.; Wu, T.; Li, Y.; Luntz, A. C.; Bajdich, M.; Cui, Y. Identifying the Active Surfaces of Electrochemically Tuned $LiCoO_2$ for Oxygen Evolution Reaction. *J. Am. Chem. Soc.* **2017**, *139*, 6270–6276.

Chapter 2. Tuning the Morphology and Electronic Properties of Single-Crystal $LiNi_{0.5}Mn_{1.5}O_{4-\delta}$: Exploring the Influence of LiCl-KCl Molten Salt Flux Composition and Synthetic Temperature

*Stephanie Spence[†], Zhengrui Xu[†], Sami Sainio[§], Dennis Nordlund[§] and Feng Lin[†]**

[†]Department of Chemistry, Virginia Tech, Blacksburg, Virginia 24061, United States

[§]Stanford Synchrotron Radiation Lightsource, SLAC National Accelerator Laboratory, Menlo Park, California 94035, United States

This chapter was submitted and accepted for publication in *Inorganic Chemistry.*[1] Reprinted with permission from American Chemical Society: Spence, S. L.; Xu, Z.; Sainio, S.; Nordlund, D.; Lin, F. Tuning the Morphology and Electronic Properties of Single-Crystal $LiNi_{0.5}Mn_{1.5}O_{4-\delta}$: Exploring the Influence of LiCl–KCl Molten Salt Flux Composition and Synthesis Temperature. *Inorg. Chem.* **2020**, *59*, 10591–10603. Copyright 2020.

2.1. Abstract

Single-crystal materials have played a unique role in the development of high performance cathode materials for Li batteries due to their favorable chemomechanical stability. The molten salt synthesis method has become one of the most prominent techniques to synthesize single-crystal layered and spinel materials. In this work, the molten salt synthesis method is used as a technique to tune both the morphology and Mn^{3+} content of high-voltage $LiNi_{0.5}Mn_{1.5}O_4$ (LNMO) cathodes. The resulting materials are thoroughly characterized by a suite of analytical techniques, including synchrotron X-ray core-level spectroscopy, which are sensitive to the materials properties at multiple length scales. The multidimensional characterization allows us to build a materials library according to the molten salt phase diagram as well as to establish the relationship between synthesis, materials properties, and battery performance. Results of this work show that Mn^{3+} content is primarily dependent on the synthesis temperature and increases as temperature is increased. Particle morphology is mostly dependent on the composition of the molten salt flux, which can be tailored to obtain well-defined octahedrons enclosed by (111) facets, plates with predominant $(11\bar{2})$ facets, irregularly shaped particles, or mixtures of these. The electrochemical measurements indicate that the Mn^{3+} content has a larger contribution to the battery performance of LNMO than morphological characteristics and that a significant amount of Mn^{3+} could become detrimental to the battery performance. However, with similar Mn^{3+} contents, morphology still plays a role in influencing the battery cycle life and rate performance. The insights of molten salt synthesis parameters on the formation of LNMO, with deconvolution of the roles of Mn^{3+} and morphology, are crucial for continuing studies in the rational design of LNMO cathode materials for high energy Li batteries.

2.2. Introduction

Today, lithium-ion batteries are ubiquitous in consumer electronics such as laptops, and cellular devices due to their high energy density and cycling performance.[2] However, further improvements in safety, energy density, and cycle life are necessary to meet the increasing demands of additional large-scale applications, such as electric vehicles.[3] High-voltage cathode materials have been investigated as possible strategies to meet these requirements. Of these, spinel $LiNi_{0.5}Mn_{1.5}O_4$ (LNMO) is one of the most promising cathode materials for lithium batteries due to its high working potential (4.7-4.9 V vs Li/Li^+), reasonable theoretical capacity (148 mAh/g), high energy density (650 Wh/kg), abundance of raw materials, and three-dimensional lithium diffusion paths leading to high rate capability.[4–6] In addition to being the most attractive feature of this material, high operating voltage can also lead to electrolyte degradation and capacity deterioration, especially at elevated temperatures, which has been a barrier to the practical application of LNMOs.[7] Fluorinated solvents such as fluoroethylene carbonate (FEC) or salt additives such as lithium bis(oxalate)borate (LiBOB) and dimethyl methylphosphonate (DMMP) have been used to improve the cycling performance compared to traditional electrolytes comprised of $LiPF_6$ salt dissolved in carbonates.[8] Furthermore, the development of solid electrolytes with high lithium-ion conductivity and stable interfaces may also solve the intrinsic issues related to high voltage operation batteries including those using LNMO.

In spinel LNMO, oxygen adopts a cubic close packed array with lithium ions occupying the tetrahedral sites and transition metals in the octahedral sites. Depending on synthesis conditions, LNMO adopts two different crystal structures.[9] An ordered phase of the space group $P4_332$ is formed when Ni and Mn ions occupy 4a and 12b Wyckoff positions, respectively.[10] This stoichiometric material has Ni^{2+} and Mn^{4+} fixed oxidation states. With high temperature

calcinations (> 700 °C), a disordered Fd$\bar{3}$m phase can be formed with Ni and Mn randomly distributed on the 16d sites.[9] In the disordered phase, non-stoichiometric LNMO can be accompanied by the presence of oxygen vacancies and/or Mn^{3+}.[11,12] The oxygen deficient material is often expressed as $LiNi_{0.5}Mn_{1.5}O_{4-\delta}$. An additional voltage plateau appears at ~ 4.0 V due to the electrochemically active Mn^{3+}, which is believed to improve performance through increased electronic conductivity and Li^{+} diffusion.[13,14] However, the presence of Mn^{3+} may also lead to Jahn Teller distortion and transition metal dissolution via the disproportionation reaction ($2Mn^{3+} \rightarrow Mn^{2+} + Mn^{4+}$), which can lead to capacity fading.[15] Formation of the disordered phase is also closely associated with the formation of rock-salt $Li_xNi_{1-x}O$-type impurities due to the high temperature synthesis conditions.[6] Fd$\bar{3}$m LNMO can be transformed to $P4_332$ with a post synthesis annealing near 700 °C, followed by slow cooling, which can restore oxygen to the lattice.[9,12,16]

Much research focus on LNMO has been on correlating material properties such as particle size and morphology, crystal structure, and Mn^{3+} content to electrochemical performance.[17–21] It is necessary to understand how experimental conditions can affect the degree of cation ordering and Mn oxidation state in LNMO for the rational design of high-voltage cathode materials. While efforts to decouple and individually study the properties of LNMO have been undertaken,[22–25] the significance of morphology versus structural ordering or Mn^{3+} content as the dominant feature in dictating performance has been debated due to the difficulty of studying each parameter in isolation. Molten salt synthesis techniques, utilizing a low melting point salt or mixture of salts as a reaction medium have been used as an effective method to precisely control the properties of LNMO.[26–28] The low melting point flux allows for increased diffusion of the reactants, improving the crystallinity of the final product. Particle size and morphology, as well as the extent of order/disorder and Mn^{3+} content can all be tuned through varying synthetic conditions including

temperature, heating duration, precursors, molten salts, and ratios of reactants and salts.[9,26,29] Kim et al. have studied the effect of calcination atmosphere, molten salt amount, synthesis temperature, and synthesis time on the formation of LNMO via molten salt synthesis.[26] Furthermore, Hai et al. have prepared octahedral and plate-like LNMO differing in Mn^{3+} content using eutectic LiCl-KCl and pure LiCl fluxes, respectively.[29] However, to the best of our knowledge, the influence of both LiCl-KCl flux composition and synthesis temperature on the LNMO formation has not yet been thoroughly studied, particularly in terms of the interrelationship between molten salt composition, temperature, crystal structure, electronic properties, morphology, and battery performance.

Herein, we have prepared a series of LNMO materials via a molten LiCl-KCl salt synthesis method. Through systematically varying the maximum synthesis temperature and the composition of the salt flux across the phase diagram from 20% LiCl to 100% LiCl (**Figure 2-1**), we can tune the melting point of the composite salt mixture, affecting the conditions of particle formation. We correlate how synthetic parameters of the molten salt method effect morphology, size, crystal structure, and electronic properties (including Mn^{3+} and oxygen deficiencies), and, in-turn, how these materials characteristics effect electrochemical performance of LNMO cathodes. This study provides a platform to study the molten salt synthesis dependent materials characteristics to inform the future rational design of LNMO cathode materials.

2.3. Experimental

2.3.1. Sample Preparation

Stoichiometric amounts of $Ni(NO_3)_2 \cdot 6H_2O$ (Sigma Aldrich) and $Mn(NO_3)_2 \cdot 4H_2O$ (Sigma Aldrich) (1:3) were dissolved in a minimum amount of deionized water. LiCl (Ward's Science) and KCl (Alfa Aesar) were added at a molar ratio of 1:30 transition metals (TM):salts. The ratio

of LiCl to KCl was varied. The mixture was ground in a mortar, then heated in a 40 mL uncovered, porcelain crucible housed in a box furnace in an air environment at a ramp rate of 2 °C/min, holding for 8 hours at the maximum desired temperature. The resultant powers were thoroughly washed with deionized water and isopropyl alcohol to remove any salt residue, then dried in a vacuum oven at 80 °C overnight to obtain approximately 1 gram of LNMO. Approximately 4% of the salt flux was lost to evaporation during heating. The low synthesis temperatures resulted in minimal evaporation, while the high TM: salt ratio makes this loss negligible in terms of the reaction media.

2.3.2. Materials Characterization

X-ray diffraction (XRD) patterns were acquired using a benchtop Rigaku Miniflex II with a Cu Kα light source (λ=1.54 Å). Patterns were collected from 10 – 80 °2θ with a step size of 0.02 °2θ and a 1.0 second count time. Fullprof software was used for structural refinement using the Rietveld method. Soft X-ray absorption spectroscopy (XAS) was performed on the 31-pole wiggler beamline 10-1 at Stanford Synchrotron Radiation Lightsource (SSRL). A ring current of 350 mA and a 1000 L/mm spherical grating monochromater with a 20 µm entrance and exit slit were used to acquire ~10^{11} ph/s at a 0.28 eV resolution in a 1 mm^2 beam spot. Data was collected under ultrahigh vacuum (10^{-9} Torr) in a single load at room temperature. Spectra were normalized by the current from freshly evaporated gold on a fine grid positioned upstream of the main chamber. Raman spectra were collected on a WITec Raman spectrometer with a 633 nm laser beam. Scanning electron microscopy (SEM) was used to investigate particle morphology using a LEO FESEM at an acceleration voltage of 5.0 kV.

2.3.3. Electrochemical Measurements

Electrodes were prepared by mixing 80 wt% LNMO active material, 10 wt% polyvinylidene fluoride (PVdF) binder, and 10 wt% carbon black conductive additive in N-methyl-2-pyrrolidone (NMP). The slurries were cast onto carbon coated aluminum foils using a doctor blade. Cathode disks with an area of 0.785 cm^2 were cut from the electrode sheets and dried in a vacuum oven at 120 °C overnight before being transferred to an argon-filled glovebox. Coin cells were assembled using CR2032 coin cell parts with Li-foils as the anode and Celgard 2400 polypropylene membranes as the separators. The electrolyte was 1 M $LiPF_6$ in 3:7 v/v ethylene carbonate (EC):dimethyl carbonate (DMC). Electrochemical measurements were carried out on a LAND battery testing system from 3.5 to 4.9 V vs. Li/Li^+. For galvanostatic charge/discharge experiments, cells were cycled at 0.1 C (1 C = 148 mAh/g). For rate capability testing, cells were cycled three times at 0.1 C, then charged at 0.1 C and discharged at different current densities.

2.4. Results and Discussion

2.4.1. Influence of molten salt composition and synthetic temperature on crystal structure and Mn^{3+} content

LNMO was synthesized using the molten salt method with different compositions of LiCl and KCl to span the phase diagram of the two salts. LiCl-KCl compositions of 100:0, 80:20, 59:41 and 40:60 were used as reaction mediums and each composition was used to synthesize materials at maximum temperatures of 650, 750, and 850 °C. A ratio of 20:80 LiCl:KCl was used to synthesize materials only at 750 and 850 °C due to the high composite melting temperature of 688 °C;[30] synthesis at 650 °C would lead to incomplete melting of the salts. The ratio of 59:41 LiCl:KCl represents the eutectic composition of LiCl and KCl in which the mixture has a minimum melting

temperature of 352 °C. In order to investigate the cation ordering and Mn reduction induced through varying synthetic parameters, no additional post-synthesis annealing was performed. **Figure 2-1** shows the synthetic points of interest along the LiCl-KCl phase diagram as well as the materials properties considered as factors dictating electrochemical performance. Selected SEM images are also shown in **Figure 2-1** to summarize the changes in particle morphology as a function of synthetic conditions.

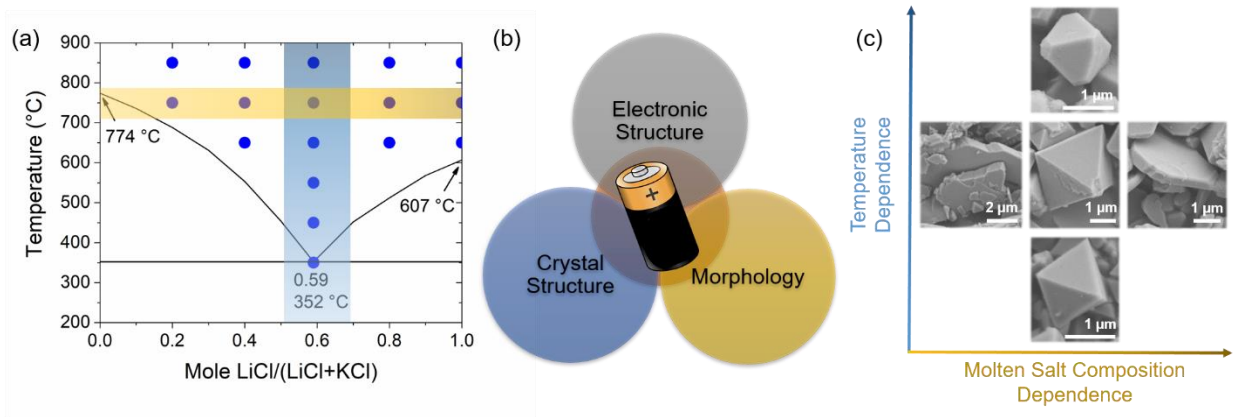

Figure 2-1. (a) LiCl-KCl phase diagram illustrating tunable synthesis parameters. (b) Materials properties influencing electrochemical performance, which are studied in the work. (c) Selected SEM images to illustrate temperature dependent and molten salt composition dependent particle morphologies. Note that the particle sizes are not representative.

To first investigate the crystal structure of the synthesized materials, powder XRD patterns were collected (**Figure A-1**). All fourteen materials of interest were indexed to the cubic $Fd\bar{3}m$ space group. A small amount of impurity phases were found to increase with the synthesis temperature. The presence of electrochemically inactive rock-salt $Li_xNi_{1-x}O$-type impurities occurs with synthesis temperatures above 700 °C, where they become thermodynamically stabilized.[31]

The crystal structure model for this space group is presented in **Figure 2-2a**, which shows that Ni and Mn cations are randomly arranged in the octahedral sites of the face centered cubic framework. Additional sub-phases such as spinel $LiMn_2O_4$ may also be present in non-trivial amounts in highly disordered samples with increased $Li_xNi_{1-x}O$ impurities due to segregation of Ni and Mn.

Rietveld refinement was performed based on a single $Fd\bar{3}m$ phase model to determine the lattice parameter, a, for each sample (**Figure 2-2b**). The full table of structural parameters obtained from the refinement analysis is displayed in **Table A-1**. **Figure 2-2c** shows the discharge profiles for the materials synthesized using the eutectic salt ratio at each temperature. The plateau at ~ 4.0 V originates from the Mn^{3+}/Mn^{4+} redox.[9] The Mn^{3+} content from each sample was approximated from the discharge profile by determining the percent of total capacity obtained from 3.8 to 4.25 V. Electrochemical performance will be discussed in detail in **Section 2.4.4**. For the materials synthesized using the eutectic ratio of LiCl-KCl, it is apparent that the 4.0 V plateau increased with increasing synthesis temperature from 650 to 850 °C. Higher synthesis temperatures may induce more oxygen vacancies, which can be compensated by the reduction of Mn.[32,33] The formation of more rock-salt $Li_xNi_{1-x}O$-type impurities may also occur during high temperature synthesis, as well as the formation of Ni-Mn oxides in the Li deficient environments.[34] The presence of these impurities can increase the Mn/Ni ratio in the disordered spinel phase, increasing the Mn^{3+} without the formation of oxygen vacancies.[11] Comparison of the lattice parameter, a, and the approximate Mn^{3+} content for the full series of materials shows that both properties increased as the synthetic temperature increased from 650 to 850 °C for each flux composition (**Figure 2-2d**). This is rationalized by the larger ionic radius of Mn^{3+} (0.65 Å) compared to Mn^{4+} (0.54 Å);[35] the increased lattice parameter in the samples suggests expansion due to higher Mn^{3+} content.[16] For example, material synthesized at 650 °C using the eutectic salt composition had a lattice

constant of 8.1581(5) Å and an average Mn^{3+} content of 5.87%. Increasing the synthesis temperature to 850 °C using the same salt media resulted in a lattice constant of 8.2167(3) Å and a Mn^{3+} content of 50.32% for the sample. The trend for sample properties was not as clear when varying the molten salt composition at a single temperature. At lower proportions of LiCl, there was a more significant increase in lattice constant and Mn^{3+} content which may be due to poorer LNMO crystal formation in this molten salt composition. The high melting temperature of 688 °C for the 20:80 LiCl:KCl flux as well as decreased Li^{+} mobility as K^{+} concentration was increased may have impacted the formation of the spinel phase.[36]

Raman spectroscopy was also used to evaluate each sample because it is sensitive to local crystal structure. It is useful to determine the degree of cation ordering in LNMO because XRD cannot detect small amounts of ordered phases due to the technique's poor chemical contrast to distinguish Ni and Mn.[37] **Figures 2-2e, 2-2f, and 2-2g** show the Raman spectra for the materials synthesized at 650, 750, and 850 °C, respectively. Peaks at 650 cm^{-1} represent the symmetric Mn-O stretching vibration in a MnO_6 octahedra while peaks at 490 and 390 cm^{-1} are assigned to the Ni^{2+}-O stretching mode.[12,23] Due to the separated Ni and Mn sites, peak spitting at about 630 cm^{-1} is expected for the lower symmetry, ordered $P4_332$ structure, as well as the appearance of additional peaks at 239, 218, and 160 cm^{-1}. Broad peaks without splitting show the predominance of the disordered spinel phase for all samples, which is consistent with XRD data (**Figure A-1**). The features of the Ni^{2+}-O stretching become less intense as the temperature increases, most noticeably for samples prepared with 20:80 LiCl:KCl at 750 and 850 °C, and with 100:0 LiCl:KCl at 850 °C indicating a greater degree of cation disorder. The sample prepared with 100:0 LiCl:KCl at 850 °C also has a noticeable peak shift likely due to the increased impurity phases. From the structural characterizations, all materials synthesized belong to the $Fd\bar{3}m$ space group. The extent

of the disorder increased with increasing temperature for each molten salt composition investigated and is coupled with the Mn^{3+} content.

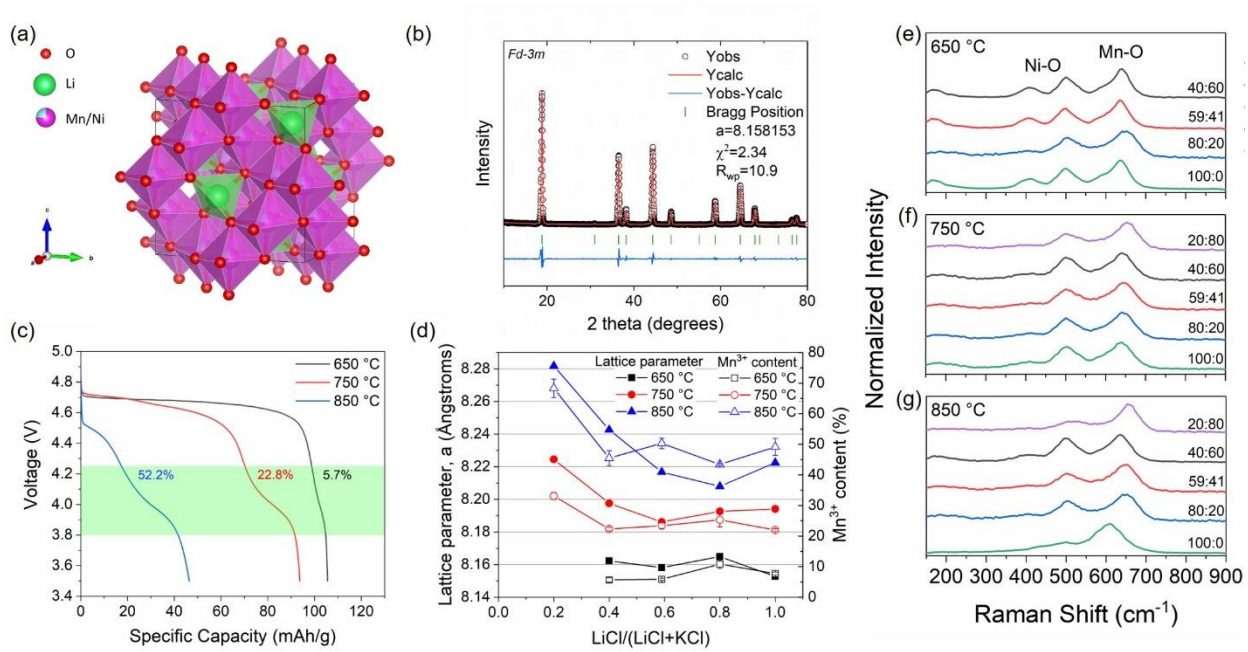

Figure 2-2. (a) Crystal structure of Fd$\bar{3}$m LNMO. (b) XRD pattern and Rietveld refinement of LNMO synthesized using eutectic LiCl-KCl at 650 °C. (c) Discharge profiles of LNMO synthesized using eutectic LiCl-KCl at 0.1 C to illustrate that the increase in synthesis temperature increases the capacity contribution in the 3.8 – 4.25 V region due to the Mn redox. (d) Comparison of lattice parameters calculated by Rietveld refinement and approximate Mn^{3+} contents to illustrate of the similarity of trends as synthesis temperature and molten salt composition are varied. (e-g) Raman spectra of LNMO prepared with different LiCl-KCl compositions at 650, 750, and 850 °C, where the ratios in the figure represents the molar ratio LiCl:KCl.

Synchrotron XAS was also performed to further characterize the electronic structure of the materials at different length scales. Soft XAS is a technique capable of probing transition metal

(TM) oxidation states and local environments in a compound with element specificity and surface sensitivity.[38] The total electron yield (TEY) detection mode probes 2-5 nm of the materials surface, while fluorescence yield (FY) mode collects signal up to 50 nm, which is still considered sub-surface for large particles in the present case. Soft XAS probes the unoccupied states through TM 2p-3d transitions at the TM L-edge and O 1s-2p transitions at the O K-edge.[31,39] The TM L-edge is divided due to spin-orbit splitting with the L_3-edge at lower energy and the L_2-edge at higher energy.

Figure 2-3a-c shows the Mn L-edges collected in the TEY mode for LNMO synthesized in different LiCl-KCl compositions at various temperatures. For Mn, the intensity ratio of the high energy and low energy L_3 shoulders is indicative of the oxidation state, with a higher ratio indicating more oxidation. A decrease in the high-to-low L_3 shoulder intensity ratio, as well as an increase in total peak areas, was seen as synthesis temperature increased, indicating Mn reduction, or, in other words, increased Mn^{3+} contribution. Varying the salt ratio at a fixed temperature resulted in a slight change of the Mn oxidation state for each temperature series, but no discernable trend appeared as the ratio was varied across the phase diagram. At 650 °C (**Figure 2-3a**) and 750 °C (**Figure 2-3b**), 80:20 LiCl:KCl produced the samples with the most reduced Mn. At 850 °C (**Figure 2-3c**), ratios of 59:41 and 100:0 LiCl:KCl led to samples with the most Mn reduction.

The Ni L-edges (**Figure 2-3d-f**) showed no change for any of the samples, indicating all pristine materials have Ni in the expected 2+ oxidation state despite the synthesis method. The O K-edge pre-edge region with sharp peaks from 527 to 534 eV originates from O-2p and TM-3d hybridization. Increasing pre-edge peak areas corresponds to increasing hybridization and should also correlate with increasing TM oxidation states.[31] For LNMO samples, total pre-edge peak areas

of the O K-edge spectra (**Figure 2-3g-i**) are generally smaller for samples that also contain Mn with lower oxidation states, confirming agreement of TM and oxygen soft XAS data.

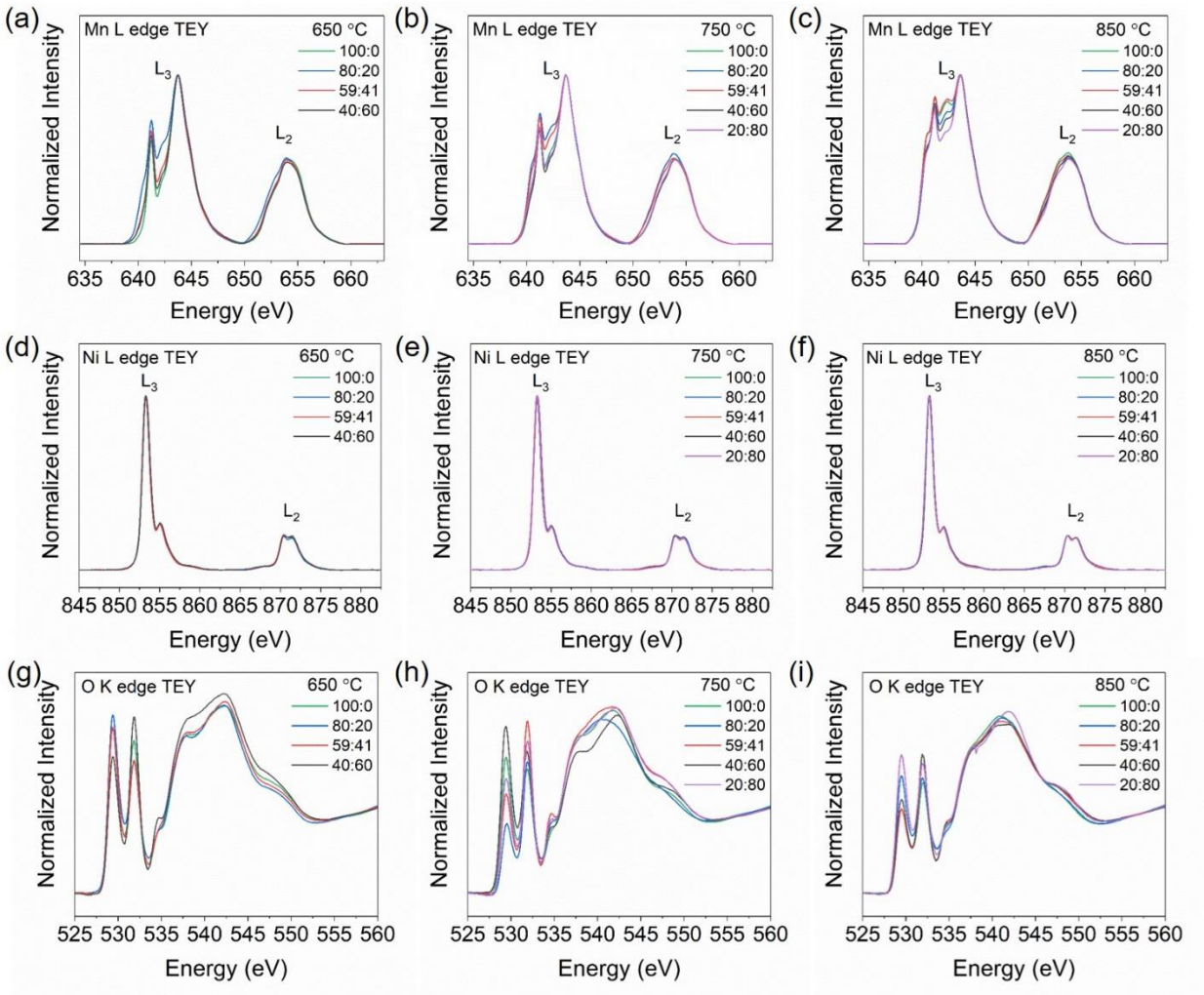

Figure 2-3. Soft XAS spectra of LNMO prepared with various LiCl-KCl compositions at fixed temperatures of (a) 650, (b) 750, and (c) 850 °C in the TEY collection mode. Mn L-edges illustrating Mn reduction at higher synthesis temperatures, and variation of the Mn oxidation state with various salt ratios at fixed synthesis temperatures. (d-f) Ni L-edges illustrating constant oxidation state, and (g-i) O K-edges illustrating decreased TM-O hybridization at higher synthesis

temperatures and variation of the TM-O hybridization with various salt ratios at fixed synthesis temperatures.

To compare the difference in the surface and sub-surface electronic states, Mn L-edge and O K-edge spectra in both the TEY and FY modes for LNMO materials synthesized using the eutectic ratio of LiCl and KCl at each temperature are shown in **Figures 2-4a** and **2-4b**. The near overlap between the TEY and FY spectra indicates similarity between surface and sub-surface Mn oxidation states for all materials, however the slightly higher intensity for the TEY mode at lower photon energy suggests the particle surfaces are slightly more reduced than the sub-surface. For the O K-edge, a similar trend of decreasing pre-edge total area is seen as temperatures increase for both detection modes. The intensity ratio of the lower energy to higher energy O K-edge pre-edge peaks also provides useful information on TM-O hybridization with lower ratios corresponding to samples with increased Mn^{3+}.[40] The intensity ratio decreases from 650 °C to 750 °C, but increases slightly from 750 °C to 850 °C; however, general trends of soft XAS data are in agreement when temperature is varied and salt ratio is fixed as well as vice versa. **Figure A-2** shows the FY spectra for the full sample set.

We performed a linear combination using a Mn_2O_3 sample as a Mn^{3+} reference and the LNMO sample containing the lowest L_3 peak area as a Mn^{4+} reference (assuming no Mn^{3+}) in the TEY collection mode in order to calculate the approximate, relative percentages of Mn^{3+} in each sample. **Figure 2-4c** displays an example spectra of the linear combination peak fitting for the LNMO sample prepared using a eutectic LiCl-KCl flux at 750 °C. We compared this approximation to the Mn^{3+} content determined from electrochemical data (previously compared to lattice parameter in **Figure 2-2d**). These results showed general agreement of the Mn^{3+} content

calculated by both methods (compare **Figures 2-2d** and **2-4d**). Discrepancies may originate from impurity content as spectroscopic methods only tell global, average oxidation state information and do not differentiate between multiple crystal structures that may be present. These impurities may be electrochemically inactive and contain mixed Mn^{3+} and Mn^{4+} states. Once again, we observed that the Mn^{3+} content increased with higher synthesis temperatures, although no clear trend was seen as LiCl-KCl compositions were varied. The electrochemical data represents a bulk analysis while soft XAS is a highly surface sensitive technique, therefore, based on our characterizations we believe the surface and the bulk electronic properties of individual samples to be generally comparable and representative.

In summary, (1) all LNMO samples were indexed by XRD to the $Fd\bar{3}m$ space group with increasing rock-salt impurities as temperatures increased. (2) Lattice constants and Mn^{3+} content both increased at higher synthesis temperatures due to the larger ionic radius of Mn^{3+} than the stoichiometric Mn^{4+}. (3) Raman spectroscopy also confirmed the $Fd\bar{3}m$ assignments, with increasing cation disorder as synthesis temperature increased. (4) Soft XAS showed that Mn was more reduced and TM-O hybridization decreased for samples prepared at higher temperatures. (5) The Mn^{3+} content approximated from both soft XAS data and electrochemical characterization was in agreement, supporting the theory that higher synthesis temperatures lead to reduction of Mn which may be induced though the presence of oxygen vacancies, excess metal cations, or impurity phases. However, (6) none of the structural characterization methods showed clear trends for samples prepared at fixed temperatures, indicating that the Mn^{3+} content is not strongly dependent on LiCl:KCl molten salt composition.

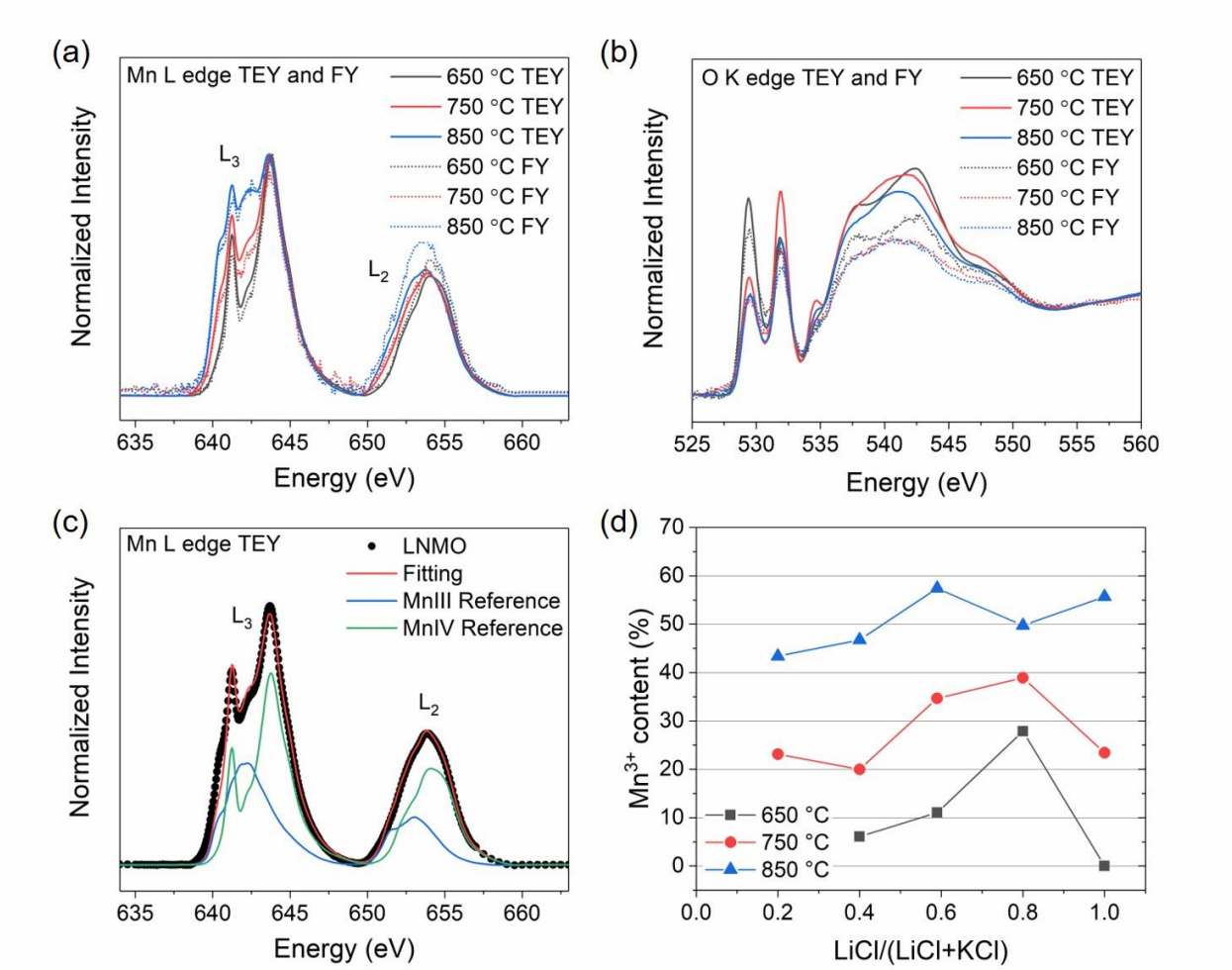

Figure 2-4. Comparison of TEY and FY collection modes for (a) Mn L-edge spectra and (b) O K-edge spectra of LNMO prepared using eutectic LiCl-KCl at 650, 750, and 850 °C. (c) Example of linear combination spectra for the LNMO sample prepared using 59:41 LiCl:KCl at 750 °C. Mn(III) reference: Mn_2O_3. Mn(IV) reference: LNMO prepared using 100:0 LiCl:KCl at 650 °C. (d) Approximate Mn^{3+} content calculated from Mn L-edge XAS fittings.

2.4.2. Influence of molten salt composition and synthetic temperature on morphology and particle size

In order to determine the influence of the molten salt composition and synthesis temperature on LNMO particle morphology and size, samples were analyzed by SEM. Each

composition and temperature combination investigated is plotted on the phase diagram of LiCl and KCl in **Figure 2-5a**. Morphological changes were most clearly seen as salt composition was varied. It has been observed with perovskite $LaMnO_3$ prepared in both eutectic LiCl-KCl and NaCl-KCl that the synthesis temperature did not change the particle morphology or size, while the change in flux had a significant effect on both.[41] This is consistent with our observations. At a fixed salt flux composition, samples appeared to have a dominant morphology independent of synthesis temperatures.

The growth rates of crystal surface differ due to differences in surface energies. The equilibrium shape of crystals is often predicted to be comprised of the lowest energy facets, however, crystals may not reach their equilibrium morphology during growth as kinetic factors dictate the final shape.[42] Reaction conditions influence nucleation and growth rates, where the ratio of these determines particle size and morphology. In molten salt methods, nucleation and growth are determined by both the melting temperature of the flux and the composite properties of the flux, including melting temperature, viscosity, ionic radii, and precursor solubility.[43] In fluxes with lower melting temperatures, there is a lower ratio between nucleation and growth rate, and as a result, larger crystals with wider size distributions are obtained.[43] Higher surface energy facets that are kinetically favorable may be stabilized in different flux environments, although the influence of the chemical properties of the flux on particle morphology have not been fully revealed.

The low melting temperature of 353 °C for the eutectic ratio of 59:41 LiCl:KCl salt facilitated the diffusion of the raw materials, allowing crystal formation and for the thermodynamically favorable morphology of octahedrons enclosed by (111) facets to predominate at a low synthetic temperature of 650 °C (**Figure 2-5c**).[26] The 40:60 mixture, in which the molar ratio of both salts is similarly balanced may have similar composite properties to the eutectic ratio

and also led to the formation of octahedrons (**Figure 2-5b**). This salt ratio has a higher melting temperature of 553 °C, only 97 °C below the 650 °C synthetic temperature, and so the nucleation to growth ratio is predicted to be higher. This led to the formation of smaller octahedron particles overall (~0.5 µm) than the eutectic composition (~1.0 µm) at 650 °C. For the lower melting temperature eutectic LiCl-KCl media, particle formation was predominantly in the liquid phase and larger particles were able to form rapidly. Particle with similar morphologies also form at 750 °C (**Figures 2-5g** and **2-5h**) and 850 °C (**Figures 2-5l** and **2-5m**) in these fluxes for the same reasons.

The flux ratios with a higher proportion of LiCl to KCl (80% LiCl in **Figures 2-5d, 2-5i,** and **2-5n** and 100% LiCl in **Figures 2-5e, 2-5j,** and **2-5o**) created favorable conditions to stabilize higher energy facets, giving rise to more kinetically driven plate-like morphologies with $(11\bar{2})$ surfaces in addition to thermodynamically stable octahedrons.[29] This is due to both the higher melting points and changes in chemical properties of the flux. Similarly, with a 20% LiCl composition at 750 and 850 °C syntheses (**Figures 2-5f** and 2-**5k**), irregular and plate-like morphologies predominated.

At a fixed salt flux composition, increasing temperatures did not affect particle size significantly. **Figure A-3** shows the size distribution histograms for each material based on the SEM images and averaging the diameter of one hundred randomly selected particles. Increasing temperature in the investigated range did not change overall particle morphology, but allowed for continued growth of already predominating facets. For example, the eutectic ratio led to the formation of octahedrons enclosed by (111) facets of approximately 1.0 µm in diameter at all temperatures 650 to 850 °C with increasing (100) truncation visible as the temperature increased (**Figures 2-5c, 2-5h,** and **2-5m**). Likewise, 100% LiCl allowed kinetically stable $(11\bar{2})$ facets to

predominate resulting in plate-like particles at all temperatures (**Figures 2-5e, 2-5j,** and **2-5o**) with the development of more (111) facets as temperatures increased, leading to thicker plates.[44,45] Increasing amounts of salt flux could be used to narrow the particle size distribution. However, large amounts of salt flux are disadvantageous as it may become more difficult to separate synthesized materials from the salt residue.[26,46]

In summary, our SEM analysis suggests that the morphology and size of LNMO synthesized by the molten salt method is more dependent on the LiCl-KCl composition than the synthetic temperature. Well-defined octahedrons, plates, and irregularly shaped particles were all synthesized through variation of the salt composition. Size distribution was also found to broaden slightly with increasing temperatures.

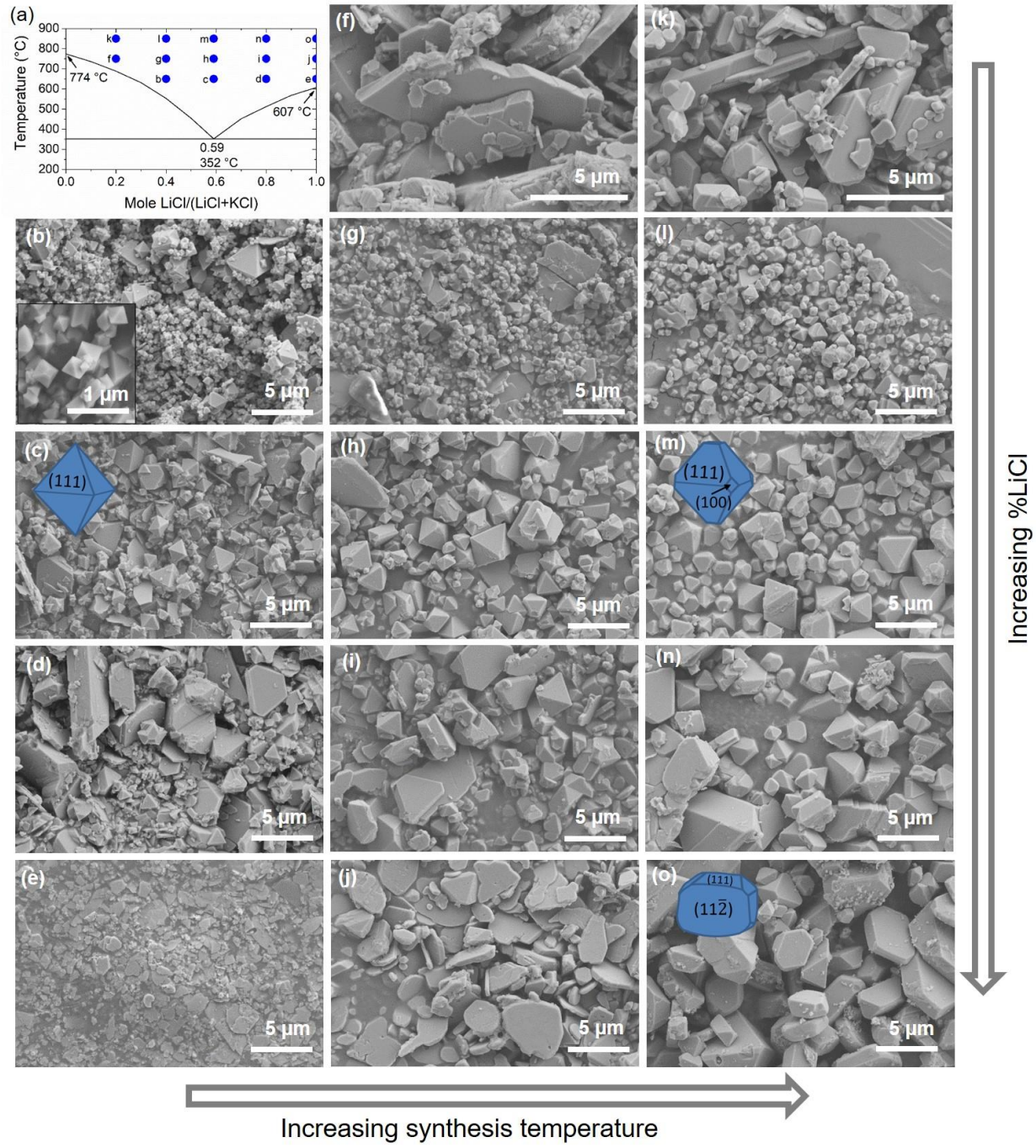

Figure 2-5. (a) LiCl-KCl phase diagram. SEM images of LNMO prepared at (b-e) 650 °C, (f-j) 750 °C, and (k-o) 850 °C with LiCl:KCl compositions of (f, k) 20:80 (irregular particles), (b, g, l) 40:60 (octahedrons), (c, h, m) 59:41 (octahedrons), (d, i, n) 80:20 (octahedrons and plates), and (e, j, o) 100:0 (plates).

2.4.3. Investigating particle formation using eutectic LiCl:KCl molten salt ratio (59:41) at different synthetic temperatures

To further investigate the low melting temperature eutectic LiCl-KCl composition on the formation of LNMO particles, material was synthesized using the eutectic flux at low synthesis temperatures of 350, 450, and 550 °C. **Figure 2-6a** compares the XRD patterns for these materials to those previously discussed, which were synthesized at 650, 750, and 850 °C. It should be noted, the synthesis at 350 °C is close to the 352 °C melting temperature for the flux, so a molten reaction may not have been complete, resulting in a very small yield of powder sample (<50 mg, that is ~5.0 % yield of a normal batch), which was not studied by XRD analysis. From the 450 °C synthesis sample, the pattern indicative of the $Fd\bar{3}m$ space group is present suggesting LNMO formation begins below this temperature. However, the 450 °C sample pattern also showed significant peaks of a Mn_2O_3 intermediate phase (indicated by dots) which occurred during the open air calcination.[47] At 550 °C, the intermediate phase decreases as the spinel phase continues to form. By 650 °C a pure phase spinel is obtained. Samples synthesized at 750 and 850 °C also show the spinel phase with increasing contributions from $Li_xNi_{1-x}O$-type impurity phases.

TEY mode Mn L-edge soft XAS spectra for low temperature synthesized samples are shown in **Figure 2-6b**. Approximate Mn^{3+} content was determined from the XAS data, as previously discussed. **Figure A-4** contains the Mn L-edge FY and Ni L-edge and O K-edge TEY and FY spectra. The change in lattice parameter, a, and the Mn^{3+} content are plotted as a function of increasing synthesis temperature in **Figure 2-6c**. The trend of increasing lattice parameter with higher temperature only holds for temperatures above 650 °C. From 450 to 650 °C, the lattice parameter is constant at ~ 8.16 Å. This is consistent with the literature as cation disordering and the introduction of Mn^{3+} are expected to occur with syntheses above 700 °C.[12] With increasing

temperature, more oxygen vacancies and impurities and, in turn, Mn^{3+} are introduced. The sample synthesized at 350 °C had a larger Mn^{3+} content than those in the 450 to 650 °C range which is likely due to the unreacted precursors containing Mn in lower oxidation states or the significant presence of Mn_2O_3, as shown by the XRD pattern (**Figure 2-6a**).

The SEM images for LNMO synthesized at low temperatures are shown in **Figures 2-6d-f**. Due to the low temperature formation of the liquid reaction media in the eutectic salt flux, the development of nanometer sized LNMO octahedrons appears to begin as low as 350 °C (**Figure 2-6d**). Micron sized, irregularly shaped particles were also visible and may be unreacted precursors or intermediate phase particles. At 450 °C (**Figure 2-6e**), thin, sheet-like crystals appeared along with the nanometer LNMO octahedrons indicating precursors or intermediates had still not completely reacted. By 550 °C (**Figure 2-6f**), well developed, micron-sized octahedrons predominated with a morphology and size comparable to the materials synthesized at 650 °C (**Figure 2-5c**).

In summary, using a low melting temperature eutectic salt mixture of LiCl and KCl allows LNMO crystal formation to begin as low as 350 °C, as soon as the molten flux is formed with pure phase, micron sized crystals fully developed by 550 °C. Increased cation disorder and Mn^{3+} content appear at synthesis temperatures above 700 °C.

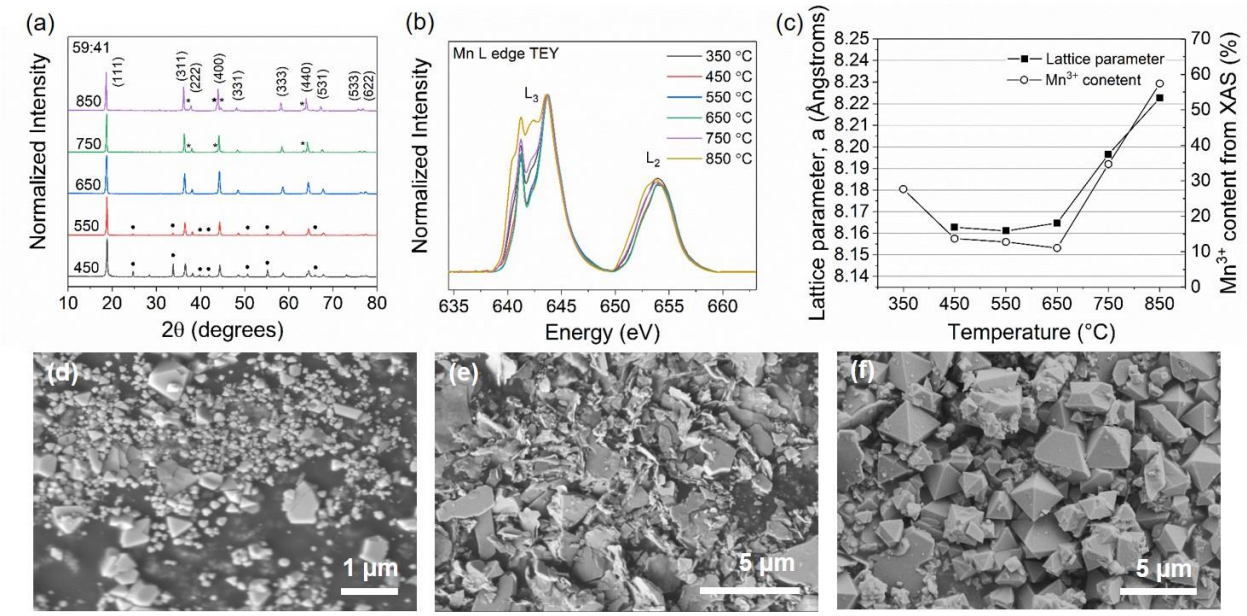

Figure 2-6. (a) XRD patterns of LNMO prepared using eutectic LiCl-KCl at various temperatures. Fd$\bar{3}$m Miller indices are labeled. Asterisks indicate location of rock-salt impurities. Dots indicate location of Mn_2O_3 intermediate phase. (b) Mn L-edge XAS spectra of LNMO prepared using eutectic LiCl-KCl at various temperatures. (c) Comparison of lattice parameter and approximate Mn^{3+} content. SEM images of LNMO synthesized in 59:41 LiCl:KCl at (d) 350, (e) 450, and (f) 550 °C.

2.4.4. Influence of molten salt composition and synthetic temperature on electrochemical performance

In order to evaluate the electrochemical performance of LNMO synthesized under different molten salt synthesis conditions, coin cells were prepared and cycled at 22 °C from 3.5 to 4.9 V under galvanostatic conditions at 0.1 C (1 C = 148 mAh/g). The first discharge profile for each material synthesized with different molten salt compositions at 650, 750, and 850 °C, is shown in **Figures 2-7a, 2-7b,** and **2-7c**, respectively. For the 650 °C synthesis series (**Figure 2-7a**), fluxes with 40, 59, and 80% LiCl produced materials with discharge capacities of 105.8, 105.6, and 107.7

mAh/g. Material synthesized with 100% LiCl gave 84.15 mAh/g initial discharge capacity. This decrease in capacity compared to the rest of the series is likely due to the significantly different morphology produced by using 100% LiCl salt flux. For the 750 °C synthesis series (**Figure 2-7b**), the eutectic ratio produced the material with the highest capacity at 93.72 mAh/g, while the 40:60 LiCl:KCl mixture produced the best performing material for the 850 °C series (**Figure 2-7c**) with a 62.3 mAh/g discharge capacity. The initial capacity obtained from samples drastically decreased with increasing synthetic temperatures. This corresponds to a significant increase in the 4.0 V plateau with increased temperature. The decrease in capacity may therefore be attributed to the increase in structural disorder and impurity phases accompanying the Mn reduction as synthetic temperatures increase.

To further illustrate this observation, dQ/dV plots are shown in **Figures 2-7d-f**. The change in Mn^{3+} content represented by the peak at 4.0 V is much more significant between the samples synthesized at various temperatures, rather than by those synthesized at a single temperature using various salt compositions. The huge variation in Mn^{3+}, determined from the percent of capacity obtained from 3.8 to 4.25 V, increases from approximately 5-10% for materials synthesized at 650 °C, to 22-33% for those synthesized at 750 °C, up to 44-68% at 850 °C synthesis. Majority of the capacity for the 650 °C synthesis series is obtained from the major voltage plateaus at ~ 4.7 V, which corresponds to the Ni^{2+}/Ni^{4+} redox process and leads to higher capacities. For the 750 and 850 °C series, the reduced contribution to the capacity from Ni redox may result from increased concentrations of electrochemically inactive Ni rock-salt impurities or an unfavorably high degree of cation disorder.

The location of peaks in the dQ/dV plots is also informative. The separation of the peaks at 4.7 V is indicative of the extent of order/disorder, where separation by > 50 mV is considered

disordered and separation of < 30 mV is considered ordered for spinel LNMO.[17] The quality of the dQ/dV plots is not high enough to confidently discern the location of these peaks, but for the 750 and 850 °C synthesis samples, increasing separation into two peaks at ~ 4.7 V is clear qualitatively, indicating a higher extent of cation disorder, which is consistent with previous structural characterizations discussed in this work.

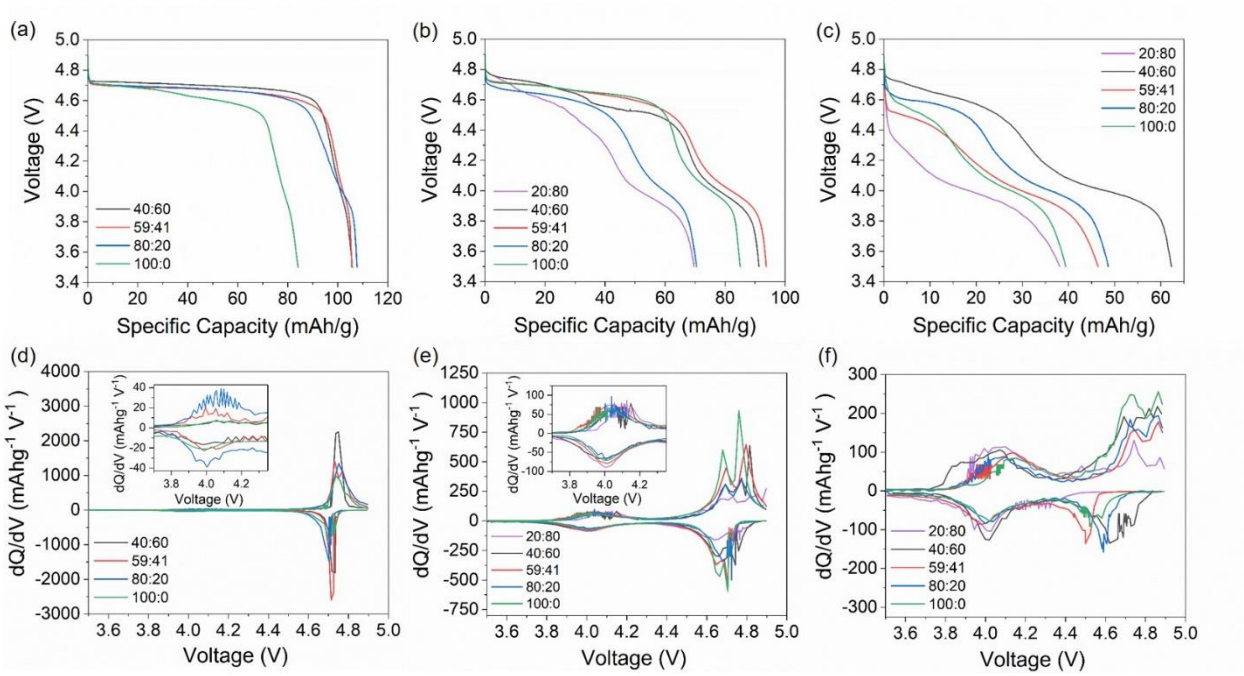

Figure 2-7. First discharge profiles of LNMO prepared with different LiCl-KCl compositions at (a) 650, (b) 750, and (c) 850 °C between 3.5 and 4.9 V at 0.1 C. The second discharge is shown for the sample prepared with 20:80 LiCl:KCl at 750 °C. dQ/dV plots for samples prepared at (d) 650, (e) 750, and (f) 850 °C. Inserts show the region between 3.7 – 4.35 V. The ratios in the figure represent the molar ratio LiCl:KCl. The measurements were performed at 22 °C.

Long term cycling data is shown is **Figures 2-8a-c**. Coin cells were cycled 100 times at a rate of 0.1 C. There is an initial increase in the capacity for nearly all samples due to

electrochemical activation.[48] After 100 cycles, all samples show high capacity retentions > 89%. The 850 °C series show the highest capacity retentions at 97.0-99.9% as a result of its much lower capacity, which reduces side reactions with the electrolyte and allows for longer reversible cycling without capacity fading. A single trend in the discharge capacity as molten salt compositions are varied is not seen for series of samples prepared at fixed temperatures. At a fixed temperature, a smaller variation in Mn^{3+} is seen compared to samples prepared at different temperatures, and increasing Mn^{3+} does not necessarily correspond to increasing capacity. The Mn^{3+} content, therefore, does not fully explain the differences in performance for material synthesized at fixed temperatures, rather, their performance differences originate from changes in morphology, size, extent of disorder, or a synergistic combination of these characteristics. **Figure A-5** shows both the charge and discharge capacities over 100 cycles, as well as the Coulombic efficiencies.

Rate capability tests were performed for all materials with 0.1 C charging and 0.1, 0.2, 0.5, 1, 2, 5, and 10 C discharge rates. Plots were normalized to the first discharge capacity after three activation cycles at 0.1 C. In the 650 °C series (**Figure 2-8d**), 80% LiCl flux gave rise to the material with the best rate performance at all C-rates, due to the slight increase of Mn^{3+} improving electronic conductivity compared to other samples in the series (**Figures 2-4d** and **2-7a**). [49,50] For the sample synthesized with 100% LiCl, less Mn^{3+} (**Figures 2-4d** and **2-7a**) and the presence of $(11\bar{2})$ facets (**Figure 2-5e**) led to inferior rate performance. Octahedrons enclosed by (111) facets are expected to have better rate capability than the $(11\bar{2})$ facet containing plates due to better Li^{+} diffusion kinetics.[29,51]

For samples synthesized at 750 °C (**Figure 2-8e**), increased Mn^{3+} content led to the highest rate capability for all samples, maintaining up to 87% of the initial capacity at 10 C for the best performing sample. The sample synthesized with 20% LiCl gave the poorest rate performance of

the series, which may be attributed to its irregular morphology and large particle size (> 2 μm) increasing the lithium diffusion path.[22] For the set of samples synthesized at 850 °C (**Figure 2-8f**), the presence of truncating (100) facets (**Figures 2-5l-n**) was expected to show improved Li^+ diffusion compared to 100% (111) facets,[23] however the significant percentage of Mn^{3+} appeared to have a detrimental effect on rate capability. This is likely due to increased impurity phases which may also be responsible for the reduced Mn. Meanwhile, the slightly smaller octahedrons synthesized with 40% LiCl (**Figure 2-5l**) give the best performance at each C-rate; nano-sized particles have improved rate performance due to smaller Li^+ diffusion pathways.[32] Irregularly shaped samples synthesized in 20% LiCl at 750 and 850 °C, and plate-like samples synthesized with 100% LiCl at 850 °C representing either end of the LiCl composition spectrum gave the poorest rate performances. The increased impurity phases, large size, and larger extend of cation disorder explain the overall low capacity and the significant loss of capacity at faster C-rates.[52]

In LNMO, Mn^{3+} is expected to be redox active and can lead to better electrochemical performance and rate capability than the perfectly stoichiometric material. More Mn^{3+} was expected to improve rate capability due to the increased lattice parameter, improving Li^+ diffusion;[53] however, the accompanying rock-salt $Li_xNi_{1-x}O$-type impurities that also occur with increased synthetic temperatures and an increase in cation disorder may have been detrimental to performance. In summary, our electrochemical data suggests that there is an optimum concentration of Mn^{3+} between ~ 10 and 25% that can improve electrochemical performance. Concentrations in this range provide increased ionic conductivities in the disordered spinel, while concentrations larger than this are likely due to a large presence of reduced Mn in segregated impurity phases. Controlled post-synthesis annealing and slow cooling to maintain Mn^{3+} but reduce impurity formation would give further insights into the isolated effects of Mn^{3+} content on

LNMO performance. It is also important to consider that larger concentrations of Mn^{3+} at the materials surface may lead to increased transition metal dissolution during high voltage operation. Further optimization of Mn^{3+} in LNMO must take dissolution behavior into account.[8]

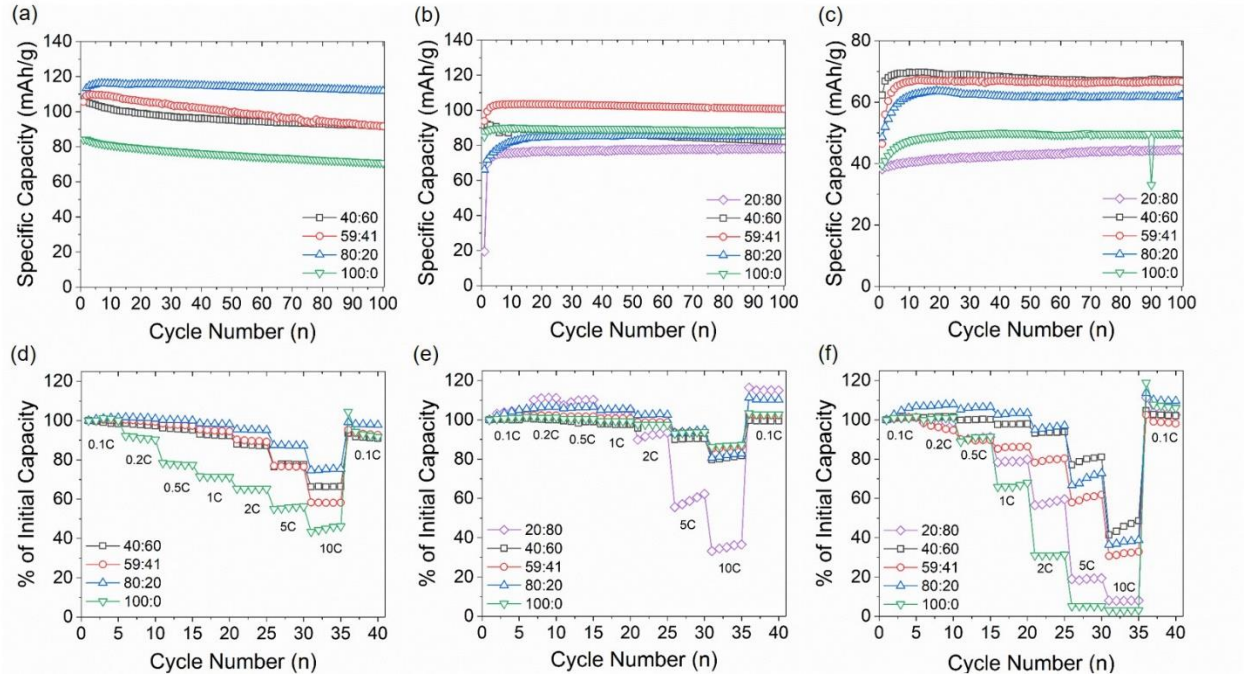

Figure 2-8. Cycling performance of LNMO prepared with different LiCl-KCl compositions at (a) 650, (b) 750, and (c) 850 °C between 3.5 and 4.9 V at 0.1 C. Rate capability with constant charging at 0.1 C and discharging at various C-rates for samples prepared at (d) 650, (e) 750, and (f) 850 °C. The ratios in the figure represent the molar ratio LiCl:KCl. The measurements were performed at 22 °C.

2.5. Conclusions

LNMO was synthesized via a molten salt method using LiCl and KCl. Synthetic parameters including molten salt composition and max synthesis temperature were carefully and systematically tuned to determine their effects on material properties and electrochemical

performance. Varying the composition of LiCl and KCl across the phase diagram, we have tuned the melting temperature of the flux medium to investigate the impact on particle formation and growth. A series of materials differing in morphology and particle size, as well as Mn oxidation states were acquired. We have identified series of materials with similar sizes and morphologies but with significantly different Mn^{3+} content ranging from ~ 7 to ~ 25 to ~ 50% that are dependent on the synthesis temperatures of 650, 750, or 850 °C, respectively. Similarly, materials with similar Mn^{3+} contents, differing in size and overall morphology are dependent on the composition of the molten salt. The change in particle morphology can therefore be attributed to the properties of the salt flux more so than the difference in the synthetic temperature above the melting temperature. A low melting temperature eutectic ratio of LiCl-KCl gave rise to thermodynamically favorable octahedrons enclosed by (111) facets forming as low as the composite melting temperature of 350 °C and developing to micron sized particles by 550 °C.

Electrochemical characterizations showed that despite increased Mn^{3+} content induced through high temperature syntheses, the accompanying high concentrations of rock-salt impurities and severe cation disorder can be detrimental to the capacity and rate performance of spinel LNMO. The sample synthesized using a salt flux of 80:20 LiCl:KCl at 650 °C showed the best performance overall with a maximum discharge capacity of 115.8 mAh/g and a capacity retention of 96.8% after 100 cycles. Its rate capability was comparable to those in the 750 °C series, with a capacity of 84 mAh/g (75% of the capacity at 0.1C) at 10 C. Between ~ 10 and 25% Mn^{3+} content may be an ideal quantity to give high capacity and improved rate capability. Over ~ 30% bulk Mn^{3+} content began to hinder the performance of LNMO as segregated impurity phases likely contributed to the large amounts of reduced Mn detected.

We have investigated several independent and coupled materials characteristics of LNMO including crystal structure, electronic structure, and morphology as molten salt synthesis parameters were systematically tuned. Molten salt synthesis methods can therefore be used to rationally design LNMO with specific facets and with controllable amounts of Mn^{3+}. Materials can be further modified through post processing techniques such as annealing to improve the electrochemical performance and minimize impurity phases. Further studies in the synthesis of LNMO are needed to continue to decouple the influence of Mn^{3+} content and its associated parameters.

2.6. References

(1) Spence, S. L.; Xu, Z.; Sainio, S.; Nordlund, D.; Lin, F. Tuning the Morphology and Electronic Properties of Single-Crystal $LiNi_{0.5}Mn_{1.5}O_{4-\delta}$: Exploring the Influence of LiCl–KCl Molten Salt Flux Composition and Synthesis Temperature. *Inorg. Chem.* **2020**, *59*, 10591–10603.

(2) Tarascon, J. M.; Armand, M. Issues and Challenges Facing Rechargeable Lithium Batteries. *Nature* **2001**, *414* (6861), 359–367.

(3) Armand, M.; Tarascon, J. M. Building Better Batteries. *Nature* **2008**, *451* (7179), 652–657.

(4) Patoux, S.; Daniel, L.; Bourbon, C.; Lignier, H.; Pagano, C.; Le Cras, F.; Jouanneau, S.; Martinet, S. High Voltage Spinel Oxides for Li-Ion Batteries: From the Material Research to the Application. *J. Power Sources* **2009**, *189* (1), 344–352.

(5) Santhanam, R.; Rambabu, B. Research Progress in High Voltage Spinel $LiNi_{0.5}Mn_{1.5}O_4$ Material. *J. Power Sources* **2010**, *195* (17), 5442–5451.

(6) Zhong, Q. Synthesis and Electrochemistry of $LiNi_xMn_{2-x}O_4$. *J. Electrochem. Soc.* **1997**, *144* (1), 205.

(7) Ma, J.; Hu, P.; Cui, G.; Chen, L. Surface and Interface Issues in Spinel $LiNi_{0.5}Mn_{1.5}O_4$: Insights into a Potential Cathode Material for High Energy Density Lithium Ion Batteries. *Chem. Mater.* **2016**, *28* (11), 3578–3606.

(8) Manthiram, A.; Chemelewski, K.; Lee, E. S. A Perspective on the High-Voltage $LiMn_{1.5}Ni_{0.5}O_4$ spinel Cathode for Lithium-Ion Batteries. In *Energy and Environmental Science*; 2014; Vol. 7, pp 1339–1350.

(9) Kim, J. H.; Myung, S. T.; Yoon, C. S.; Kang, S. G.; Sun, Y. K. Comparative Study of

$LiNi_{0.5}Mn_{1.5}O_{4-\delta}$ and $LiNi_{0.5}Mn_{1.5}O_4$ Cathodes Having Two Crystallographic Structures: Fd3m and P4332. *Chem. Mater.* **2004**, *16* (5), 906–914.

(10) Julien, C. M.; Mauger, A. Review of 5-V Electrodes for Li-Ion Batteries: Status and Trends. *Ionics (Kiel).* **2013**, *19* (7), 951–988.

(11) Aktekin, B.; Valvo, M.; Smith, R. I.; Sørby, M. H.; Lodi Marzano, F.; Zipprich, W.; Brandell, D.; Edström, K.; Brant, W. R. Cation Ordering and Oxygen Release in $LiNi_{0.5-x}Mn_{1.5+x}O_{4-y}$ (LNMO): In Situ Neutron Diffraction and Performance in Li Ion Full Cells. *ACS Appl. Energy Mater.* **2019**, *2* (5), 3323–3335.

(12) Song, J.; Shin, D. W.; Lu, Y.; Amos, C. D.; Manthiram, A.; Goodenough, J. B. Role of Oxygen Vacancies on the Performance of $Li[Ni_{0.5-x}Mn_{1.5+x}]O_4$ (x = 0, 0.05, and 0.08) Spinel Cathodes for Lithium-Ion Batteries. *Chem. Mater.* **2012**, *24* (15), 3101–3109.

(13) Jafta, C. J.; Mathe, M. K.; Manyala, N.; Roos, W. D.; Ozoemena, K. I. Microwave-Assisted Synthesis of High-Voltage Nanostructured $LiMn_{1.5}Ni_{0.5}O_4$ Spinel: Tuning the Mn^{3+} Content and Electrochemical Performance. *ACS Appl. Mater. Interfaces* **2013**, *5* (15), 7592–7598.

(14) Xiao, J.; Chen, X.; Sushko, P. V.; Sushko, M. L.; Kovarik, L.; Feng, J.; Deng, Z.; Zheng, J.; Graff, G. L.; Nie, Z.; Choi, D.; Liu, J.; Zhang, J.-G.; Whittingham, M. S. High-Performance $LiNi_{0.5}Mn_{1.5}O_4$ Spinel Controlled by Mn^{3+} Concentration and Site Disorder. *Adv. Mater.* **2012**, *24* (16), 2109–2116.

(15) Yi, T. F.; Mei, J.; Zhu, Y. R. Key Strategies for Enhancing the Cycling Stability and Rate Capacity of $LiNi_{0.5}Mn_{1.5}O_4$ as High-Voltage Cathode Materials for High Power Lithium-Ion Batteries. *J. Power Sources* **2016**, *316*, 85–105.

(16) Zheng, J.; Xiao, J.; Yu, X.; Kovarik, L.; Gu, M.; Omenya, F.; Chen, X.; Yang, X. Q.; Liu,

J.; Graff, G. L.; Whittingham, M. S.; Zhang, J. G. Enhanced Li^+ Ion Transport in $LiNi_{0.5}Mn_{1.5}O_4$ through Control of Site Disorder. *Phys. Chem. Chem. Phys.* **2012**, *14* (39), 13515–13521.

(17) Cabana, J.; Casas-Cabanas, M.; Omenya, F. O.; Chernova, N. A.; Zeng, D.; Whittingham, M. S.; Grey, C. P. Composition-Structure Relationships in the Li-Ion Battery Electrode Material $LiNi_{0.5}Mn_{1.5}O_4$. *Chem. Mater.* **2012**, *24* (15), 2952–2964.

(18) Cabana, J.; Zheng, H.; Shukla, A. K.; Kim, C.; Battaglia, V. S.; Kunduraci, M. Comparison of the Performance of $LiNi_{1/2}Mn_{3/2}O_4$ with Different Microstructures. *J. Electrochem. Soc.* **2011**, *158* (9), A997.

(19) Lin, H. B.; Zhang, Y. M.; Rong, H. B.; Mai, S. W.; Hu, J. N.; Liao, Y. H.; Xing, L. D.; Xu, M. Q.; Li, X. P.; Li, W. S. Crystallographic Facet- and Size-Controllable Synthesis of Spinel $LiNi_{0.5}Mn_{1.5}O_4$ with Excellent Cyclic Stability as Cathode of High Voltage Lithium Ion Battery. *J. Mater. Chem. A* **2014**, *2* (30), 11987–11995.

(20) Cai, Y.; Huang, S. Z.; She, F. S.; Liu, J.; Zhang, R. L.; Huang, Z. H.; Wang, F. Y.; Wang, H. E. Facile Synthesis of Well-Shaped Spinel $LiNi_{0.5}Mn_{1.5}O_4$ Nanoparticles as Cathode Materials for Lithium Ion Batteries. *RSC Adv.* **2016**, *6* (4), 2785–2792.

(21) Xiao, J.; Chen, X.; Sushko, P. V.; Sushko, M. L.; Kovarik, L.; Feng, J.; Deng, Z.; Zheng, J.; Graff, G. L.; Nie, Z.; Choi, D.; Liu, J.; Zhang, J.-G.; Whittingham, M. S. High-Performance $LiNi_{0.5}Mn_{1.5}O_4$ Spinel Controlled by Mn^{3+} Concentration and Site Disorder. *Adv. Mater.* **2012**, *24* (16), 2109–2116.

(22) Shu, Y.; Xie, Y.; Yan, W.; Meng, S.; Sun, D.; Jin, Y.; He, K. Synergistic Effect of Surface Plane and Particle Sizes on the Electrochemical Performance of $LiNi_{0.5}Mn_{1.5}O_4$ Cathode Material via a Facile Calcination Process. *J. Power Sources* **2019**, *433*, 226708.

(23) Liu, H.; Zhang, X.; He, X.; Senyshyn, A.; Wilken, A.; Zhou, D.; Fromm, O.; Niehoff, P.; Yan, B.; Li, J.; Muehlbauer, M.; Wang, J.; Schumacher, G.; Paillard, E.; Winter, M.; Li, J. Truncated Octahedral High-Voltage Spinel $LiNi_{0.5}Mn_{1.5}O_4$ Cathode Materials for Lithium Ion Batteries: Positive Influences of Ni/Mn Disordering and Oxygen Vacancies. *J. Electrochem. Soc.* **2018**, *165* (9), A1886–A1896.

(24) Casas-Cabanas, M.; Kim, C.; Rodríguez-Carvajal, J.; Cabana, J. Atomic Defects during Ordering Transitions in $LiNi_{0.5}Mn_{1.5}O_4$ and Their Relationship with Electrochemical Properties. *J. Mater. Chem. A* **2016**, *4* (21), 8255–8262.

(25) Duncan, H.; Hai, B.; Leskes, M.; Grey, C. P.; Chen, G. Relationships between Mn^{3+} Content, Structural Ordering, Phase Transformation, and Kinetic Properties in $LiNi_xMn_{2-x}O_4$ Cathode Materials. *Chem. Mater.* **2014**, *26* (18), 5374–5382.

(26) Kim, J. H.; Myung, S. T.; Sun, Y. K. Molten Salt Synthesis of $LiNi_{0.5}Mn_{1.5}O_4$ Spinel for 5 V Class Cathode Material of Li-Ion Secondary Battery. *Electrochim. Acta* **2004**, *49* (2), 219–227.

(27) Wen, L.; Lu, Q.; Xu, G. Molten Salt Synthesis of Spherical $LiNi_{0.5}Mn_{1.5}O_4$ Cathode Materials. *Electrochim. Acta* **2006**, *51* (21), 4388–4392.

(28) Börner, M.; Niehoff, P.; Vortmann, B.; Nowak, S.; Winter, M.; Schappacher, F. M. Comparison of Different Synthesis Methods for $LiNi_{0.5}Mn_{1.5}O_4$—Influence on Battery Cycling Performance, Degradation, and Aging. *Energy Technol.* **2016**, *4* (12), 1631–1640.

(29) Hai, B.; Shukla, A. K.; Duncan, H.; Chen, G. The Effect of Particle Surface Facets on the Kinetic Properties of $LiMn_{1.5}Ni_{0.5}O_4$ Cathode Materials. *J. Mater. Chem. A* **2013**, *1* (3), 759–769.

(30) Basin, A. S.; Kaplun, A. B.; Meshalkin, A. B.; Uvarov, N. F. The LiCl-KCl Binary

System. *Russ. J. Inorg. Chem.* **2008**, *53* (9), 1509–1511.

(31) Qiao, R.; Wray, L. A.; Kim, J. H.; Pieczonka, N. P. W.; Harris, S. J.; Yang, W. Direct Experimental Probe of the Ni(II)/Ni(III)/Ni(IV) Redox Evolution in $LiNi_{0.5}Mn_{1.5}O_4$ Electrodes. *J. Phys. Chem. C* **2015**, *119* (49), 27228–27233.

(32) Kunduraci, M.; Al-Sharab, J. F.; Amatucci, G. G. High-Power Nanostructured $LiMn_{2-x}Ni_xO_4$ High-Voltage Lithium-Ion Battery Electrode Materials: Electrochemical Impact of Electronic Conductivity and Morphology. *Chem. Mater.* **2006**, *18* (15), 3585–3592.

(33) Sushko, P. V.; Rosso, K. M.; Zhang, J. G.; Liu, J.; Sushko, M. L. Oxygen Vacancies and Ordering of D-Levels Control Voltage Suppression in Oxide Cathodes: The Case of Spinel $LiNi_{0.5}Mn_{1.5}O_{4-\delta}$. *Adv. Funct. Mater.* **2013**, *23* (44), 5530–5535.

(34) Xue, Y.; Han, Y.; Wang, Z. B.; Zheng, L. L.; Yu, F. Da; Zhou, Y. X. Study on $LixNi_{0.5}Mn_{1.5}O_4$ (x = 0.8, 0.9, 1, 1.1, and 1.2) High-Voltage Cathode for Lithium-Ion Batteries. *Ionics (Kiel).* **2018**, *24* (11), 3317–3323.

(35) Shannon, R. D. Revised Effective Ionic Radii and Systematic Studies of Interatomic Distances in Halides and Chalcogenides. *Acta Crystallogr. Sect. A* **1976**, *32* (5), 751–767.

(36) Lantelme, F.; Turq, P. Ionic Dynamics in the LiCl-KCl System at Liquid State. *J. Chem. Phys.* **1982**, *77* (6), 3177–3187.

(37) Amdouni, N.; Zaghib, K.; Gendron, F.; Mauger, A.; Julien, C. M. Structure and Insertion Properties of Disordered and Ordered $LiNi_{0.5}Mn_{1.5}O_4$ Spinels Prepared by Wet Chemistry. *Ionics (Kiel).* **2006**, *12* (2), 117–126.

(38) Lin, F.; Liu, Y.; Yu, X.; Cheng, L.; Singer, A.; Shpyrko, O. G.; Xin, H. L.; Tamura, N.; Tian, C.; Weng, T.-C.; Yang, X.-Q.; Meng, Y. S.; Nordlund, D.; Yang, W.; Doeff, M. M. Synchrotron X-Ray Analytical Techniques for Studying Materials Electrochemistry in

Rechargeable Batteries. *Chem. Rev.* **2017**, *117* (21), 13123–13186.

(39) Suntivich, J.; Hong, W. T.; Lee, Y. L.; Rondinelli, J. M.; Yang, W.; Goodenough, J. B.; Dabrowski, B.; Freeland, J. W.; Shao-Horn, Y. Estimating Hybridization of Transition Metal and Oxygen States in Perovskites from o k -Edge X-Ray Absorption Spectroscopy. *J. Phys. Chem. C* **2014**, *118* (4), 1856–1863.

(40) De Groot, F. M. F.; Grioni, M.; Fuggle, J. C.; Ghijsen, J.; Sawatzky, G. A.; Petersen, H. Oxygen 1s X-Ray-Absorption Edges of Transition-Metal Oxides. *Phys. Rev. B* **1989**, *40* (8), 5715–5723.

(41) Vradman, L.; Zana, J.; Kirschner, A.; Herskowitz, M. Synthesis of $LaMnO_3$ in Molten Chlorides: Effect of Preparation Conditions. *Phys. Chem. Chem. Phys.* **2013**, *15* (26), 10914–10920.

(42) Susman, M. D.; Pham, H. N.; Zhao, X.; West, D. H.; Chinta, S.; Bollini, P.; Datye, A. K.; Rimer, J. D. Synthesis of NiO Crystals Exposing Stable High-Index Facets. *Angew. Chemie Int. Ed.* **2020**, anie.202003390.

(43) Meir, R.; Vradman, L.; Zana, J.; Herskowitz, M. Effect of Salt Type on the Particle Size of $LaMn_{1-X}Fe_xO_3$ ($0.1 \leq x \leq 0.5$) Synthesized in Molten Chlorides. *Mater. Chem. Phys.* **2019**, *231*, 181–187.

(44) Chemelewski, K. R.; Li, W.; Gutierrez, A.; Manthiram, A. High-Voltage Spinel Cathodes for Lithium-Ion Batteries: Controlling the Growth of Preferred Crystallographic Planes through Cation Doping. *J. Mater. Chem. A* **2013**, *1* (48), 15334–15341.

(45) Chemelewski, K. R.; Shin, D. W.; Li, W.; Manthiram, A. Octahedral and Truncated High-Voltage Spinel Cathodes: The Role of Morphology and Surface Planes in Electrochemical Properties. *J. Mater. Chem. A* **2013**, *1* (10), 3347–3354.

(46) Hyun Yoon, K.; Soo Cho, Y.; Heon Kangs, D. Review Molten Salt Synthesis of Lead-Based Relaxors. *J. MATE RIALS Sci.* **1998**, *33*, 2977–2984.

(47) Yang, X.; Tang, W.; Kanoh, H.; Ooi, K. Synthesis of Lithium Manganese Oxide in Different Lithium-Containing Fluxes. *J. Mater. Chem.* **1999**, *9* (10), 2683–2690.

(48) Zhou, J.; Hong, D.; Wang, J.; Hu, Y.; Xie, X.; Fang, H. Electronic Structure Variation of the Surface and Bulk of a $LiNi_{0.5}Mn_{1.5}O_4$ Cathode as a Function of State of Charge: X-Ray Absorption Spectroscopic Study. *Phys. Chem. Chem. Phys.* **2014**, *16* (27), 13838–13842.

(49) Xue, Y.; Han, Y.; Yu, H. X.; Shu, J.; Wang, Z. B.; Zheng, L. L.; Xia, Y. F. Improving Rate Performance of High-Voltage Spinel Cathode by Changing Structural Evolution from Two-Phase to Solid-Solution Reactions. *Electrochim. Acta* **2018**, *281*, 24–30.

(50) Han, Y.; Xue, Y.; Xia, Y. F.; Zhang, J. N.; Yu, F. Da; Gu, D. M.; Wang, Z. B. Design of Synergistic-Coated Layer of La_2O_3/Al_2O_3 in LiNi0.5Mn1.5O4 Cathode for Enhanced Cycling Stability and Rate Capability. *Ionics (Kiel).* **2019**, *25* (6), 2459–2468.

(51) Liu, H.; Wang, J.; Zhang, X.; Zhou, D.; Qi, X.; Qiu, B.; Fang, J.; Kloepsch, R.; Schumacher, G.; Liu, Z.; Li, J. Morphological Evolution of High-Voltage Spinel $LiNi_{0.5}Mn_{1.5}O_4$ Cathode Materials for Lithium-Ion Batteries: The Critical Effects of Surface Orientations and Particle Size. *ACS Appl. Mater. Interfaces* **2016**, *8* (7), 4661–4675.

(52) Zhou, M.; Gong, J.; Deng, Z.; Lang, Y.; Zong, B.; Guo, J.; Wang, L. Synthesis and Electrochemical Performances of $LiNi_{0.5}Mn_{1.5}O_4$ Spinels with Different Surface Orientations for Lithium-Ion Batteries. *Ionics (Kiel).* **2019**, *26*, 2187–2200.

(53) Yang, J.; Han, X.; Zhang, X.; Cheng, F.; Chen, J. Spinel $LiNi_{0.5}Mn_{1.5}O_4$ cathode for

Rechargeable Lithiumion Batteries: Nano vs Micro, Ordered Phase ($P4_332$) vs Disordered Phase ($Fd\bar{3}m$). *Nano Res.* **2013**, *6* (9), 679–687.

Chapter 3. Continuously Tunable $Li_{1-x}Ni_{0.5}Mn_{1.5}O_{4-\delta}$ Supports for Metal Catalysts through Li Intercalation Chemistry

3.1. Abstract

Supported metal catalysts, a class of heterogeneous catalysts, exhibit improved catalytic performance including activities, selectivities, and lifetimes compared to unsupported nano-metal catalysts due to the introduction of unique support interactions. The properties of the support, including electronic structure and crystal facets, play a role in determining the strength and nature of these interactions. The lack of support materials with independently tunable electronic and crystal structures has created challenges to study the underlying origin of support interactions. Li containing transition metal oxides including $LiNi_{0.5}Mn_{1.5}O_4$ (LNMO) represent a class of intercalation materials which can be structurally tuned through synthetic methods and electronically tuned by utilizing Li intercalation chemistry. In this work, we have utilized a molten salt method to synthesize well-structured spinel LNMO with faceted morphologies. We then deposited size controlled gold nanoparticles on the support material's surface. Finally, we used NO_2BF_4 for chemical delithiation which can controllably remove Li from the material lattice, tuning the TM-3d orbital occupancy. Determination of catalytic mechanisms and electronic behavior is performed through monitoring the catalytic efficiency of the reduction of 4-nitrophenol. This model reaction provides a redox platform to investigate the support properties as functions of Li intercalation chemistry. Preliminary results suggest there is an optimum degree of Li deficiency that can enhance the catalytic properties of the composite catalyst. Using a variety of imaging, diffraction, and spectroscopic techniques, we studied the structural and electronic properties of LNMO at the atomic level to begin to make quantitative conclusions about support

interactions and effects. This work also provides a potential new application for recycled transition metal oxide battery cathode materials for use as catalyst supports.

3.2. Introduction

Supported metal nanocatalysts are a class of heterogeneous catalysts used for chemical upgrading. Converting fuels such as alkanes to alcohols, ketones, and aldehydes is desirable for industrial and energy storage processes but necessitates the use of a catalyst for large scale applications. Catalysts provide alternative reaction pathways with lower activation energy than uncatalyzed reactions, making the catalytic process kinetically favorable. Overall, it is estimated that catalysts contribute to one-sixth of the value of all manufactured goods in industrialized countries.[1] Supported metal catalysts exhibit improved catalytic performance including activities, selectivities, and lifetimes compared to their unsupported counterparts due to support interactions.[2] Furthermore, alteration of a support's morphology and orbital occupancy can impact the strength and nature of these interactions.[3]

Noble metals such as platinum, palladium, ruthenium, rhodium, and iridium have been widely used as heterogeneous catalysts in the petrochemical industry, medicine production, environmental protection, and energy technology.[4] However, the high price and low abundance of these noble metals cannot keep up with today's increasing demand. It has become more necessary to reduce the volume of metals used in industrial catalytic processes by maximizing surface area and atom efficiency through immobilizing metal nanocatalysts on support materials. In 1978, while studying the chemisorption properties of noble metals on metal oxide surfaces, Tauster et al. first coined the term "strong metal-support interaction" to refer to the nature of the bonding interactions between the metal oxide support and the metal.[2,5] In this study, interaction of group

VIII metals supported on TiO_2 were described by the binding between the noble metal and Ti cations. Adsorption of hydrogen was used to determine the particle sizes and sorption properties. The ability to chemisorb hydrogen was suppressed or vanished when the metals were supported on TiO_2. Such features were seen only to occur at the interface between the metal and the support. These studies suggest that studying heterogeneous catalysis from a surface analysis perspective is necessary to elucidate the origins of support effects.

Lithium (Li) containing transition metal oxides (TMO) represent a class of intercalation materials which can be structurally tuned through synthetic methods[6] and electronically tuned by utilizing Li intercalation chemistry to influence TM-3d orbital occupacny[7,8]. Typically used for energy storage as battery cathodes, the ability to intercalate and extract Li ions also makes these materials useful as tunable catalyst supports. Through Li removal, the orbital occupancy and TM−O covalency of the materials can be tuned.[9] In addition, utilizing battery cathode materials as catalyst supports is a potential opportunity to repurpose battery materials which have lifetimes in digital products of only one to three years.[10]

Spinel $LiNi_{0.5}Mn_{1.5}O_4$ (LNMO) is ideal for supported catalyst studies because of its three-dimensional structurally stability. LNMO exhibits two crystal structures which can be obtained depending on the synthesis method: an ordered primitive simple cubic ($P4_332$) with Mn and Ni ions occupying two separate octahedral sites and a disordered face centered cubic spinel ($Fd\bar{3}m$) where Mn and Ni ions are in a random arrangement in the octahedral sites.[11] Synthesis of the disordered phase leads to oxygen vacancies which may lead to the reduction of a small amount of inactive Mn^{4+} to Mn^{3+} in order to compensate for oxygen loss.[12,13] This redox-active Mn^{3+} slightly improves electronic conductivity and Li diffusion.[14,15] The presence of two phases of LNMO offer

an additional avenue to easily tune the TM electronic states in the pristine material during synthesis.

Support effects have been hypothesized to originate from many factors, including, but not limited to, facet or electronic effects. However, the phenomenon of support interactions is currently not well understood due to the lack of independently and continuously tunable morphological and electronic structures of support materials. LNMO represents a model candidate to study support effects and can be prepared with tunable morphology, orbital occupancy, and TM-O covalency through Li doping chemistry. The metal-support effects, and in turn, redox performance of the material, will be influenced by the surface crystal facets and orbital occupancy of the support. In this work, we combine the ability to tune the morphology of LNMO through a facile molten salt synthesis method with the electronic control achieved through chemical delithiation in order to design a conceptually new family of gold (Au) nanocatalysts supported on LNMO supports. We monitor redox activity through the reduction of p-nitrophenol, a widely used model reaction to evaluate the performance of Au nanocatalysts. We employ surface science techniques to study the structural and electronic properties at the atomic level in the hopes of revealing information about the metal-support interface and support effects. Complete control over the size, shape, and orbital occupancy of the material would be a major advancement in the field of heterogeneous catalysts as such control can be used to further tune the catalytic activity, rate, or selectivity of composite catalysts.

3.3. Experimental

3.3.1. Materials Synthesis

To synthesize the LNMO support, stoichiometric amounts of $Ni(NO_3)_2 \cdot 6H_2O$ and $Mn(NO_3)_2 \cdot 4H_2O$ (1:3) were dissolved in a minimum amount of deionized water. LiCl and KCl were added at a molar ratio of 1:30 transition metals (TM):salts. A eutectic ratio of 59:41 LiCl:KCl was used to synthesize octahedrons and pure LiCl was used to synthesize plates. The mixture was ground in a mortar, then heated in an uncovered alumina crucible housed in a box furnace at a ramp rate of 2 °C/min, holding for 8 hours at 650 °C for the octahedrons and at 750 °C for the plates. Powders were then thoroughly washed with deionized water and isopropyl alcohol to remove salt residue, and then dried in a vacuum oven at 80 °C overnight.

Au was deposited on LNMO at 2 mol % loading. First, 1 mL of 0.0048 M $HAuCl_4$ and 4 mL H_2O were added dropwise to the support which was suspended in approximately 50 mL of DI water. The solution was stirred at 80 °C for 4-6 hours or until approximately 80% of the water had evaporated, allowing Au^{3+} to chemically adsorb to the LNMO surface. The particles were then isolated and a low temperature (150 °C) annealing was performed in order to reduce Au^{3+} to Au^0. An oxygen environment was used to minimize lattice oxygen loss from the LNMO support.

Chemical delithiation was performed by stirring stoichiometric amounts of 0.1 M NO_2BF_4 dissolved in CH_3CN with the composite catalyst powders. For example, for a 20% theoretical delithiation, 20 mol% NO_2BF_4 was used. Powders were stirred at room temperature for 24 hours in loosely capped vials, then washed with CH_3CN to remove NO_2BF_4 and to stop the reaction with Li, and finally dried in a vacuum oven at 80 °C overnight.

3.3.2. Materials Characterization

The X-ray diffraction (XRD) patterns were acquired on beamline 11-3 at Stanford Synchrotron Radiation Lightsource (SSRL). The 2θ scale was converted to the corresponding angles with λ=1.5406 Å, the wavelength of Cu Kα radiation. Scanning electron microscopy (SEM) was used to investigate particle morphology using a FEI Quanta 600 FEG. Transmission electron microscopy (TEM) images were collected using a JEOL 2100 TEM. Soft X-ray absorption spectroscopy (XAS) was performed on the 31-pole wiggler beamline 10-1 at SSRL. A ring current of 350 mA and a 1000 L/mm spherical grating monochromater with a 20 µm entrance and exit slit were used to acquire ~10^{11} ph/s at a 0.28 eV resolution in a 1 mm^2 beam spot. Data was collected under ultrahigh vacuum (10^{-9} Torr) in a single load at room temperature. Spectra were normalized by the current from freshly evaporated gold on a fine grid positioned upstream of the main chamber. UV-VIS spectra were collected using an Ocean Optics Flame mini spectrometer.

3.3.3. Catalytic Reduction of p-Nitrophenol

The reduction of p-nitrophenol was performed in a stirred 4 mL quartz cuvette and monitored by UV-VIS spectroscopy. For each sample, 1 mL of 0.2 mM p-nitrophenol, 900 µL DI water, and 800 µL catalyst slurry (0.3125 mg/mL), were added to the cuvette. Then, 300 µL $NaBH_4$ in DI water (5 mg/mL) was quickly added and time resolved UV-VIS spectra were acquired until the absorbance signal at 400 nm reached a minimum.

3.4. Results and Discussion

3.4.1. Synthesis and Characterization of LNMO Support

The support effects present in composite catalyst materials can be influenced by the crystal facets of the support. Catalytic performance can therefore be correlated to the exposed crystal planes of the support. In this study, we first sought to synthesize LNMO support materials with controllable surface facets by utilizing a molten salt synthesis method. Hai et al. reported the successful synthesis of LNMO octahedrons and plate-like single-crystal particles using salt fluxes of LiCl and KCl, and pure LiCl, respectively.[6] Using a similar procedure, we synthesized LNMO in a eutectic ratio of LiCl:KCl (59:41) at a low temperature of 650 °C and in pure LiCl at 750 °C to produce octahedrons and plate-like particles. Both were held for 8 hours at the maximum temperature. The increase in temperature to 750 °C for the LNMO synthesized in pure LiCl ensures the raw materials are able to completely melt above the 607 °C melting temperature of the salt. **Figure 3-1 a** shows the phase diagram of LiCl and KCl. As the composition of the salt flux and the temperatures are changed, the properties of the molten flux including solubility, melting temperature, and viscosity are altered which, in turn, influence the morphology of the resultant particles.[16]

After synthesizing the materials, XRD was collected to determine the crystal structure. LNMO can be synthesized with an ordered $P4_332$ or disordered $Fd\bar{3}m$ crystal structure.[11] XRD patterns for materials synthesized in LiCl-KCl and in pure LiCl are shown in **Figure 3-1 b**. Both materials were indexed to the cubic $Fd\bar{3}m$ space group. A small amount of electrochemically inactive rock-salt $Li_xNi_{1-x}O$-type impurities was also found and is indicated by asterisks on the XRD patterns. These impurities are typical in $Fd\bar{3}m$ disordered spinel LNMO and are

thermodynamically stabilized at synthesis temperatures above 700 °C.[17] The impurity amount is minimal due to the low temperature syntheses.

Samples were analyzed by SEM to verify the particle morphology. The low melting temperature at 353 °C for the eutectic LiCl-KCl salt mixture allowed for efficient diffusion of the precursors, enhancing crystal formation and resulting in the thermodynamically stable octahedron morphology enclosed by (111) facets (**Figures 3-1 c** and **e**).[18] Meanwhile, the pure LiCl flux created conditions more favorable to stabilize higher energy facets resulting in plate-like particles (**Figures 3-1 d** and **f**) with predominate $(11\bar{2})$ surfaces.[6] The plates are slightly larger than the octahedrons on average, but both materials exhibit size distributions from hundreds of nanometers to 3-4 microns.

Ultimately, the molten salt synthesis method is an effective tool to tune the crystal facets and morphology of LNMO. It may also be used to tune the degree of transition metal ordering in the crystal structure; however in the present work, we focus on the $Fd\bar{3}m$ disordered LNMO. Through simply adjusting the composition of the molten salt and temperature, we have produced materials with the same crystal structure and similar sizes, only differing in morphology.

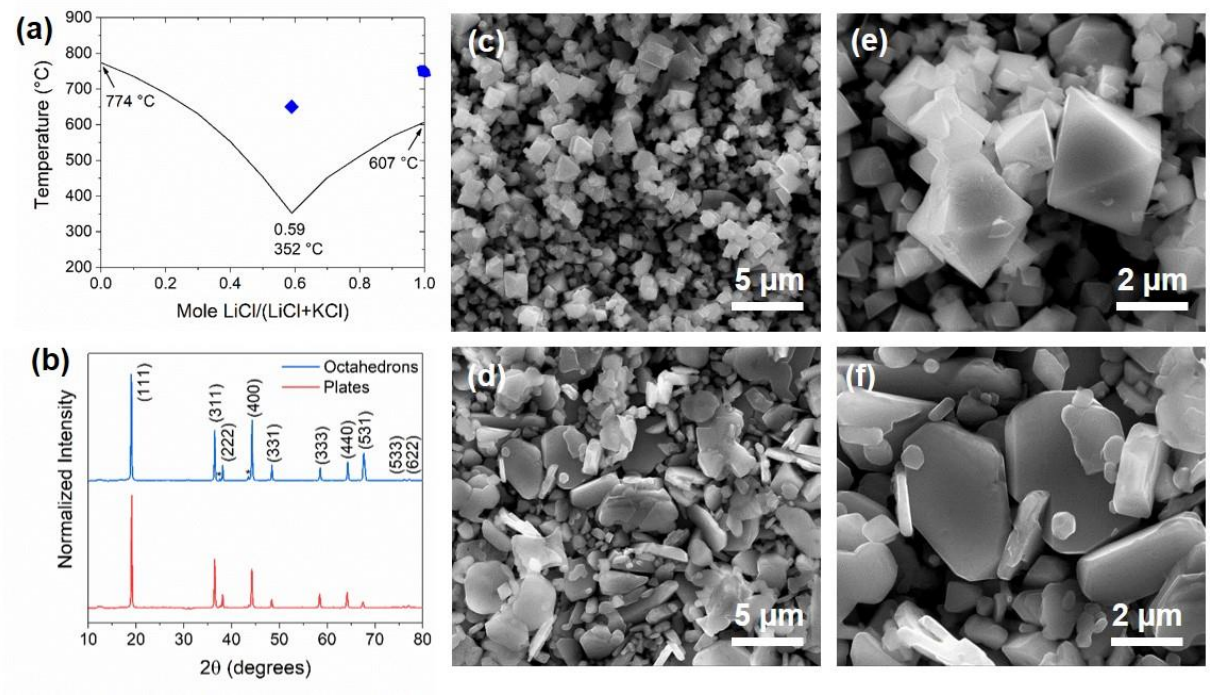

Figure 3-1. (a) LiCl-KCl phase diagram. Synthetic points of interest are plotted. (b) XRD patterns of LNMO octahedrons and plates. Fd$\bar{3}$m Miller indices are labeled. Asterisks indicate location of rock-salt impurities. SEM images of LNMO (c) and (e) octahedrons and (d) and (f) plates.

3.4.2. Au Deposition and Chemical Delithiation

To form a composite catalyst, we deposited Au nanoparticles on the support surfaces by stirring the LNMO with $HAuCl_4$ at 2 mol % loading and performing a low temperature annealing to reduce Au. We then collected TEM images to quantify the Au size distribution. A TEM of the surface of an octahedron LNMO particle after Au deposition is shown in **Figure 3-2 a**. From the image analysis, we determined the Au has a 1.83 ± 0.63 nm average diameter (**Figure 3-2 b**). This is consistent with Au particles or clusters in the size range where catalytic activity should be observed.[19] A TEM image of a corner of the octahedron support shows that Au does not appear to preferentially deposit on edges or corners (**Figure 3-2 c**). Instead, a distribution of particles across

both the edges and surface of the support is seen. Fast Fourier transform (FFT) analysis of this image shows a spot pattern we are able to index to the {011} planes of the ordered phase spinel (**Figure 3-2 d**). Samples likely contain region of both ordered and disordered spinel, but the small amount of the ordered phase is not distinguishable in the XRD. Another TEM image of the octahedron surface with higher magnification of the Au particles is shown in **Figure 3-2 e** with selected regions showing individual particles outlined in red boxes. FFTs of these selected regions are displayed in **Figure 3-2 f** and show spot patterns which we have indexed to the Au {111} planes, confirming the presence of the typical face centered cubic structure of Au metal.

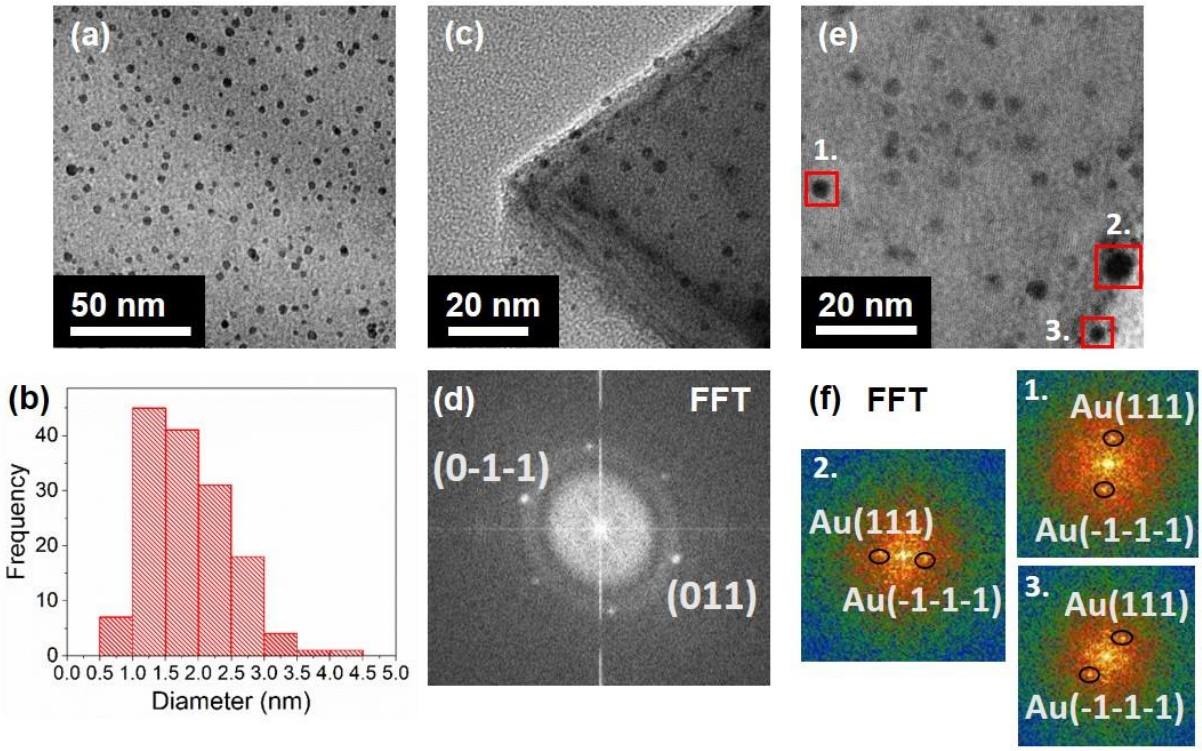

Figure 3-2. (a) TEM image of Au nanoparticles on LNMO octahedron surface and (b) Au particle size histogram with 1.83 ± 0.63 nm average particle diameter, where 148 particles are counted. (c) TEM image Au nanoparticles on LNMO octahedron depicting support edge. (d) FFT of (c) showing diffraction due to the spinel phase. (e) TEM image Au nanoparticles on LNMO

octahedron surface and (f) FFTs of regions in (e) (red boxes) showing diffraction of Au nanoparticles. Images are colored to help distinguish contrast.

After formation of the composite catalysts, we performed a chemical delithiation. Chemical delithiation methods can be used to controllably remove Li and tune TM-3d orbital occupancy in transition metal oxides. We utilized NO_2BF_4 as an oxidizing agent. By adjusting the stoichiometric ratio of the oxidizing agent to Li, we can controllably remove Li from the support structure. The advantage of this method is it is continuously tunable as we can remove Li in intervals of 1/the theoretical capacity of the material. For a baseline study, we explored various levels of delithiation using ratios of 20, 40, 60, 80, and 100% NO_2BF_4 to Li with the octahedral supports and 20, 60, and 100% NO_2BF_4 to Li with the plate-like supports. Delithiation occurs according to the reaction: $LiNi_{0.5}Mn_{1.5}O_4 + xNO_2BF_4 \rightarrow Li_{1-x}Ni_{0.5}Mn_{1.5}O_4 + xNO_2 + xLiBF_4$.

After delithiation, we monitored the surface electronic changes of the catalyst using soft XAS. This technique is able to probe the TM oxidation states with element specificity and surface sensitivity.[20] Collection in the total electron yield (TEY) detection mode can probe 2-5 nm of the material surface. Unoccupied electronic states are probed through TM 2p-3d transitions at the TM L-edge and through O 1s-2p transitions at the O K-edge.[17,21] Spin-orbit splitting divides the TM L-edges with L_3-edges at a lower energy and L_2-edges at higher energy.

For both octahedrons and plates, the Ni L-edges shows oxidation of Ni on the material surface as the delithiation degree increases, as indicated by the increase of intensity on the high energy shoulders of the L_3 edges (**Figure 3-3**). The Mn L-edges remain mostly stable in the 4+ oxidation state, which is expected as Mn^{4+} should be electrochemically inactive in this material (**Figure 3-4**). Slight oxidation of Mn is seen due to the small amount of Mn^{3+} which is present in

the disordered phase spinel accompanying the possible introduction of oxygen vacancies. The pre-edge region of the O K-edge from 527 to 534 eV originates from O-2p and TM-3d hybridization and an increase in the pre-edge peak areas corresponds to increased hybridization.[17] The O K-edges for both morphologies of LNMO shows an overall slight increase in pre-edge areas as delithiation degree increases, indicating increasing TM-O hybridization (**Figure 3-5**). This corresponds with the increasing TM oxidation. However, the differences in oxidation states for each of the samples are slight, showing we are not removing a significant amount of Li.

In summary, composite catalysts can be formed through deposition of nanometer sized Au on LNMO supports. Chemical delithiation was performed using NO_2BF_4, however, the current procedure does not give the expected theoretical Li removal. Further optimization of the delithiation procedure is required for continuously tunable Li removal. Nevertheless, our preliminary experiments suggest that, with careful control, chemical delithiation can be a viable method to tune the Li content and TM oxidation states of LNMO.

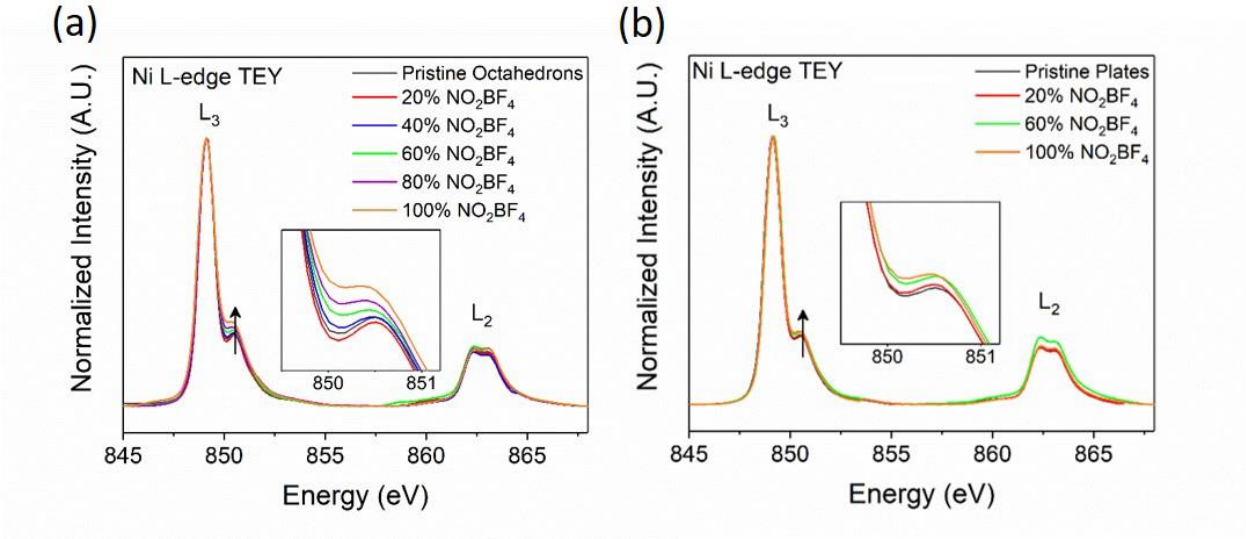

Figure 3-3. Soft XAS spectra in the TEY collection mode for LNMO delithiated with various ratios of NO_2BF_4. Ni L-edges of (a) octahedrons and (b) plates illustrating oxidation as NO_2BF_4 ratio is increased.

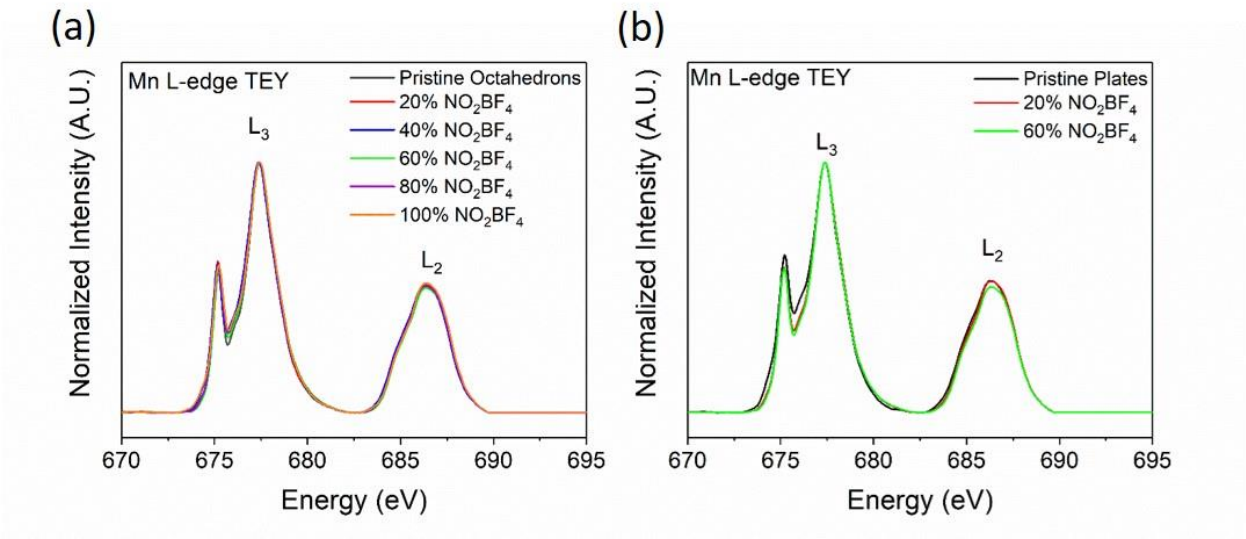

Figure 3-4. Soft XAS spectra in the TEY collection mode for LNMO delithiated with various ratios of NO_2BF_4. Mn L-edges of (a) octahedrons and (b) plates illustrating constant oxidation state as NO_2BF_4 ratio is increased.

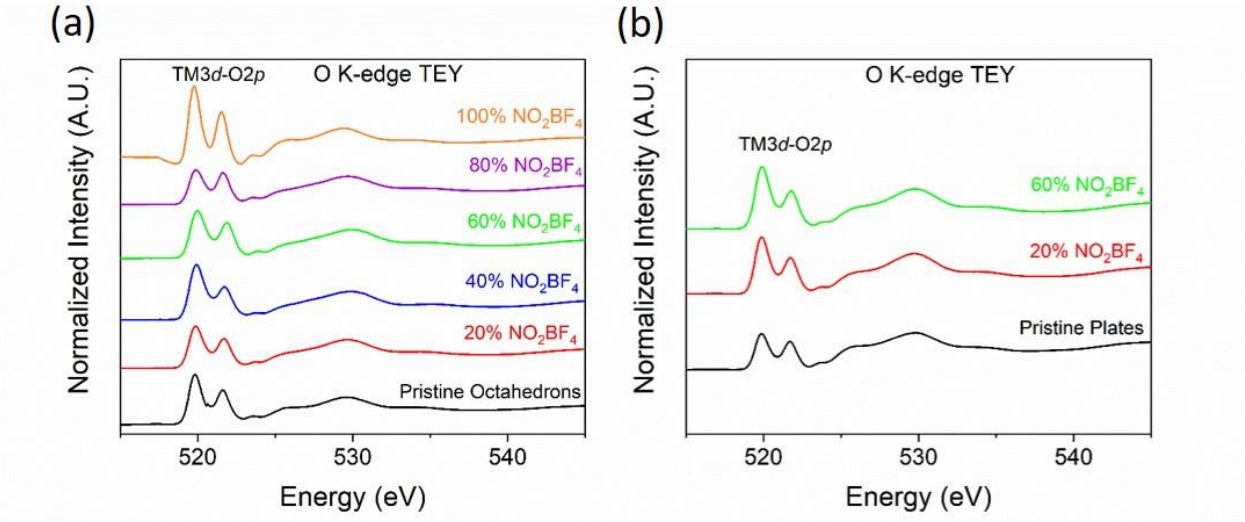

Figure 3-5. Soft XAS spectra in the TEY collection mode for LNMO delithiated with various ratios of NO_2BF_4. O K-edges of (a) octahedrons and (b) plates illustrating increasing TM-O hybridization as NO_2BF_4 ratio is increased.

3.4.3. p-Nitrophenol Model Catalytic Reaction Study

In order to examine how orbital occupancy influences catalytic performance, we can perform model catalytic reactions including the p-nitrophenol reduction to monitor redox activity of the LNMO octahedral composite catalysts at various degrees of delithiation. Catalytic activity should be dependent on the support's surface facets and TM-3d orbital occupancy. In the reaction, p-nitrophenol is reduced to p-aminophenol by sodium borohydride catalyzed by Au. This reaction is widely used as a model system to evaluate the properties of Au nanoparticles because it yields a single product from a single reactant, does not proceed in the absence of a catalyst, and the absorption of both the reactant and product occur in the visible region and can be monitored by UV-VIS spectrometry.[22,23]

To perform the reaction, we combine p-nitrophenol, water, and sodium borohydride, with 10 mol% of the active catalyst and monitor the absorbance of the nitrophenolate anion at 400 nm as it converts to 4-aminophenol at ~ 295 nm as a function of time. **Figure 3-6 a** shows the typical absorption spectra as a function of increasing reaction time. Plotting the absorbance at 400 nm versus time (**Figure 3-6 b**), the intensity decay is clearly visualized. The initial period where no change in absorbance value is observed is referred to as the induction time and is believed to be attributed to a surface-restructuring of the particles to render them catalytically active.[24] The region of time where the reaction occurs can be fit to pseudo-first order kinetics to determine the rate constant by plotting $-\ln(A_0/A)$ versus time. The kinetic constant, k, relates to the surface reactivity of the adsorbed species.[25] **Figure 3-6 c** shows the first order kinetics for selected samples averaging three trials. The pristine LNMO octahedrons without Au deposited have a rate constant of 0.1611 ± 0.0265 min^{-1} indicating that the TMO surface is itself slightly reductive. After Au deposition, the rate constant remains nearly the same at 0.2093 ± 0.0504 min^{-1} suggesting a minimum enhancement from Au alone. At 20% theoretical delithiation, the rate constant increases to 0.7620 ± 0.0366 min^{-1}, however, at 40% theoretical delithiation, the rate constant decreases to 0.4166 ± 0.0590 min^{-1}.

These preliminary results suggest that the support itself plays a role in the reaction and that there is an optimum degree of delithiation of the octahedral LNMO that will give a maximum catalytic rate of p-nitrophenol reduction. Delithiation helps to render the material more catalytically active. As Li is removed from the material, Ni is oxidized. With more Li removal, it becomes difficult to further oxidize the material during the reaction. We can continue to examine additional samples including LNMO with various morphologies and with a larger range of

delithiation degrees in order to make unambiguous conclusions about the influence of support effects.

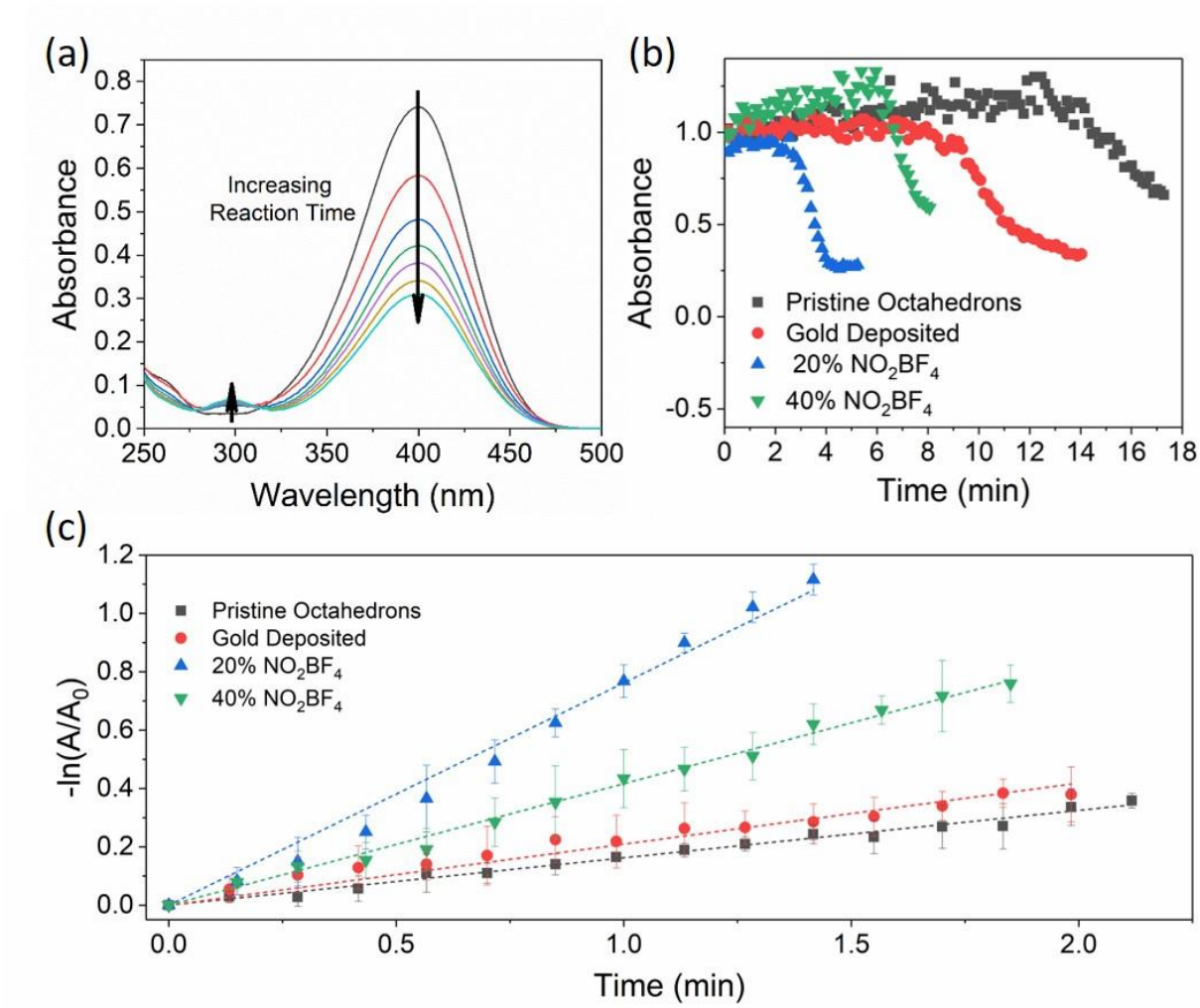

Figure 3-6. (a) Typical UV-VIS spectra of p-nitrophenol with increasing reaction time showing the p-nitrophenol peak at 400 nm decay and the 4-aminophenol peak at 295 nm increase. (b) Absorbance intensity of the 400 nm peak (p-nitrophenol) as a function of reaction time. (c) Absorbance data during the reaction period fit to pseudo-first order kinetics with respect to p-nitrophenol to determine rate constants.

3.5. Conclusions

In conclusion, LNMO, a typical battery cathode material, has been synthesized with defined facets in both octahedral and plate-like morphologies using a molten salt synthesis method. Composite supported nanocatalysts were formed by Au deposition on the TMO surface. Chemical delithiation using NO_2BF_4 has been used to tune electronic properties of the materials through Li removal, although actual removal was far less than theoretical values. Investigation of the effect of delithiation on the octahedral supports was performed through catalytic performance of the p-nitrophenol reduction model reaction. A 20% theoretical delithiation of LNMO octahedrons gave a significant catalytic enhancement while 40% theoretical delithiation gave a much smaller enhancement, suggesting the TMO support is active in the reaction and that Li removal within this range will give an optimum increase in catalytic activity. Ultimately, with its high structural stability and Li intercalation properties, LNMO is a tunable platform for continued studies in the origin of support effects. Much more work is needed, including synthesizing and characterizing a complete database of LNMO materials with various morphologies and crystal facets and degrees of delithiation to quantitatively explain the relationship between facet/*d*-orbital occupancy and catalytic results in order to decouple and identify the origins of support effects. Additional model reactions, such as oxidation reactions to complement the p-nitrophenol reduction study would offer insights on the full redox properties of the catalysts. This study also offers a potential unique avenue for the recycling of spent LIB cathode materials.

3.6. References

(1) Duward Shiver, Mark Weller, Tina Overton, Jonathan Rourke, F. A. *Inorganic Chemistry*, Sixth Edit.; W. H. Freeman and Company: New York, NY, 2014.

(2) Tauster, S. J.; Fung, S. C.; Garten, R. L. Strong Metal-Support Interactions. Group 8 Noble Metals Supported on TiO_2. *J. Am. Chem. Soc.* **1978**, *100* (1).

(3) Zhou, K.; Li, Y. Catalysis Based on Nanocrystals with Well-Defined Facets. *Angew. Chemie - Int. Ed.* **2012**, *51* (3), 602–613.

(4) Suxia, L.; Ce, H.; Yantao, S. The Power of Single-Atom Catalysis. *ChemCatChem* **2015**, *7* (17), 2559–2567.

(5) Tauster, S. J. Strong Metal-Support Interactions. *Acc. Chem. Res.* **1987**, *20* (11), 389–394.

(6) Hai, B.; Shukla, A. K.; Duncan, H.; Chen, G. The Effect of Particle Surface Facets on the Kinetic Properties of $LiMn_{1.5}Ni_{0.5}O_4$ Cathode Materials. *J. Mater. Chem. A* **2013**, *1* (3), 759–769.

(7) Wang, H.; Xu, S.; Tsai, C.; Li, Y.; Liu, C.; Zhao, J.; Liu, Y.; Yuan, H.; Abild-Pedersen, F.; Prinz, F. B.; Nørskov, J. K.; Cui, Y. Direct and Continuous Strain Control of Catalysts with Tunable Battery Electrode Materials. *Science* **2016**, *354* (6315), 1031–1036.

(8) Colligan, N.; Augustyn, V.; Manthiram, A. Evidence of Localized Lithium Removal in Layered and Lithiated Spinel $Li_{1-x}CoO_2$($0 \leq x \leq 0.9$) under Oxygen Evolution Reaction Conditions. *J. Phys. Chem. C* **2015**, *119* (5), 2335–2340.

(9) Lu, Z.; Wang, H.; Kong, D.; Yan, K.; Hsu, P.-C.; Zheng, G.; Yao, H.; Liang, Z.; Sun, X.; Cui, Y. Electrochemical Tuning of Layered Lithium Transition Metal Oxides for Improvement of Oxygen Evolution Reaction. *Nat. Commun.* **2014**, *5* (1), 4345.

(10) Zheng, X.; Zhu, Z.; Lin, X.; Zhang, Y.; He, Y.; Cao, H.; Sun, Z. A Mini-Review on Metal

Recycling from Spent Lithium Ion Batteries. *Engineering* **2018**, *4* (3), 361–370.

(11) Kim, J. H.; Myung, S. T.; Yoon, C. S.; Kang, S. G.; Sun, Y. K. Comparative Study of $LiNi_{0.5}Mn_{1.5}O_{4-\delta}$ and $LiNi_{0.5}Mn_{1.5}O_4$ Cathodes Having Two Crystallographic Structures: Fd3m and P4332. *Chem. Mater.* **2004**, *16* (5), 906–914.

(12) Aktekin, B.; Valvo, M.; Smith, R. I.; Sørby, M. H.; Lodi Marzano, F.; Zipprich, W.; Brandell, D.; Edström, K.; Brant, W. R. Cation Ordering and Oxygen Release in $LiNi_{0.5-x}Mn_{1.5+x}O_{4-y}$ (LNMO): In Situ Neutron Diffraction and Performance in Li Ion Full Cells. *ACS Appl. Energy Mater.* **2019**, *2* (5), 3323–3335.

(13) Song, J.; Shin, D. W.; Lu, Y.; Amos, C. D.; Manthiram, A.; Goodenough, J. B. Role of Oxygen Vacancies on the Performance of $Li[Ni_{0.5-x}Mn_{1.5+x}]O_4$ (x = 0, 0.05, and 0.08) Spinel Cathodes for Lithium-Ion Batteries. *Chem. Mater.* **2012**, *24* (15), 3101–3109.

(14) Jafta, C. J.; Mathe, M. K.; Manyala, N.; Roos, W. D.; Ozoemena, K. I. Microwave-Assisted Synthesis of High-Voltage Nanostructured $LiMn_{1.5}Ni_{0.5}O_4$ Spinel: Tuning the Mn^{3+} Content and Electrochemical Performance. *ACS Appl. Mater. Interfaces* **2013**, *5* (15), 7592–7598.

(15) Xiao, J.; Chen, X.; Sushko, P. V.; Sushko, M. L.; Kovarik, L.; Feng, J.; Deng, Z.; Zheng, J.; Graff, G. L.; Nie, Z.; Choi, D.; Liu, J.; Zhang, J.-G.; Whittingham, M. S. High-Performance $LiNi_{0.5}Mn_{1.5}O_4$ Spinel Controlled by Mn^{3+} Concentration and Site Disorder. *Adv. Mater.* **2012**, *24* (16), 2109–2116.

(16) Meir, R.; Vradman, L.; Zana, J.; Herskowitz, M. Effect of Salt Type on the Particle Size of $LaMn_{1-x}Fe_xO_3$ ($0.1 \leq x \leq 0.5$) Synthesized in Molten Chlorides. *Mater. Chem. Phys.* **2019**, *231*, 181–187.

(17) Qiao, R.; Wray, L. A.; Kim, J. H.; Pieczonka, N. P. W.; Harris, S. J.; Yang, W. Direct

Experimental Probe of the Ni(II)/Ni(III)/Ni(IV) Redox Evolution in $LiNi_{0.5}Mn_{1.5}O_4$ Electrodes. *J. Phys. Chem. C* **2015**, *119* (49), 27228–27233.

(18) Kim, J. H.; Myung, S. T.; Sun, Y. K. Molten Salt Synthesis of $LiNi_{0.5}Mn_{1.5}O_4$ Spinel for 5 V Class Cathode Material of Li-Ion Secondary Battery. *Electrochim. Acta* **2004**, *49* (2), 219–227.

(19) Liu, L.; Corma, A. Metal Catalysts for Heterogeneous Catalysis: From Single Atoms to Nanoclusters and Nanoparticles. *Chem. Rev.* **2018**, *118* (10), 4981–5079.

(20) Lin, F.; Liu, Y.; Yu, X.; Cheng, L.; Singer, A.; Shpyrko, O. G.; Xin, H. L.; Tamura, N.; Tian, C.; Weng, T.-C.; Yang, X.-Q.; Meng, Y. S.; Nordlund, D.; Yang, W.; Doeff, M. M. Synchrotron X-Ray Analytical Techniques for Studying Materials Electrochemistry in Rechargeable Batteries. *Chem. Rev.* **2017**, *117* (21), 13123–13186.

(21) Suntivich, J.; Hong, W. T.; Lee, Y. L.; Rondinelli, J. M.; Yang, W.; Goodenough, J. B.; Dabrowski, B.; Freeland, J. W.; Shao-Horn, Y. Estimating Hybridization of Transition Metal and Oxygen States in Perovskites from o k -Edge X-Ray Absorption Spectroscopy. *J. Phys. Chem. C* **2014**, *118* (4), 1856–1863.

(22) Zhao, P.; Feng, X.; Huang, D.; Yang, G.; Astruc, D. Basic Concepts and Recent Advances in Nitrophenol Reduction by Gold- and Other Transition Metal Nanoparticles. *Coord. Chem. Rev.* **2015**, *287*, 114–136.

(23) Chakraborty, S.; Ansar, S. M.; Stroud, J. G.; Kitchens, C. L. Comparison of Colloidal versus Supported Gold Nanoparticle Catalysis. *J. Phys. Chem. C* **2018**, *122* (14), 7749–7758.

(24) Wunder, S.; Lu, Y.; Albrecht, M.; Ballauff, M. Catalytic Activity of Faceted Gold Nanoparticles Studied by a Model Reaction: Evidence for Substrate-Induced Surface

Restructuring. *ACS Catal.* **2011**, *1* (8), 908–916.

(25) Wunder, S.; Polzer, F.; Lu, Y.; Mei, Y.; Ballauff, M. Kinetic Analysis of Catalytic Reduction of 4-Nitrophenol by Metallic Nanoparticles Immobilized in Spherical Polyelectrolyte Brushes. *J. Phys. Chem. C* **2010**, *114* (19), 8814–8820.

Chapter 4. Conclusions and Outlooks

In this work, single-crystal LNMO has been synthesized though a molten salt synthesis method. Careful tuning of synthetic properties including salt composition and synthesis temperature have had a drastic influence on the properties of the resultant materials. Changes to particle morphology and Mn oxidation state were thoroughly characterized and investigated. The impact of these changes to chemical properties including electrochemical performance were investigated. LNMO was also used as a nanocatalysts support and the influence of delithiation on the catalytic rate of p-nitrophenol reduction was preliminarily explored. Through this work, we have reiterated that the molten salt synthesis offers a facile method to tune morphological and electronic properties of LNMO and have determined that LNMO properties are highly influenced by the extent of Mn^{3+} in the global composition. This work provides insights into the rational design of LNMO for improved electrochemical performance in LIBs or as catalyst supports to provide a method to recycle spent battery cathode materials.

While this work explores several properties of LNMO, there are additional parameters and questions concerning single-crystal LNMO that are still of interest for examination in future work. For example, we have shown that Mn^{3+} content is dependent on synthesis temperature, but also wish to determine the distribution of Mn oxidation state within a single particle. Preliminary transmission X-ray microscopy (TXM) analysis of LNMO synthesized using a eutectic LiCl-KCl flux at 650 and 850 °C (**Figure 4-1**) suggests that the surface of the particles are slightly more oxidized than the bulk, in contrast to our soft XAS measurements which is likely due to the difference of probing depth and surface sensitivity of the two techniques. We strive to continue to explore and explain the origin of the distribution of Mn oxidation states as well as local lattice

strain within single particles as a function of both synthesis temperature, particle morphology, and particle size through X-ray nano-diffraction studies.

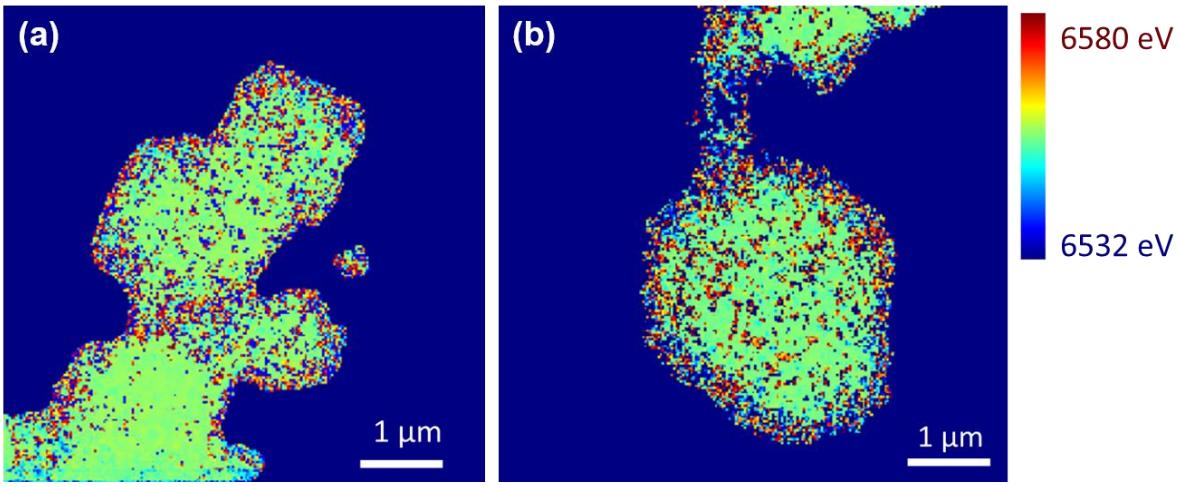

Figure 4-1. 2D TXM image of LNMO synthesized using eutectic LiCl-KCl at (a) 650 °C and (b) 850 °C showing Mn K-edge energy. Color bar shows low edge energy (low valance state) in blue to high edge energy (high valance state) in red.

The progression of this work will move toward utilizing the molten salt method to synthesize and understand the properties of a broad range of single-crystal cathode materials. In addition to spinel LNMO, the methods outlined in this work may be applied to the synthesis and characterization of single-crystal layered TM oxide cathodes such as NMC and NCA in both Li-ion and Na-ion batteries. Ultimately, there are many avenues to continue to explore in single-crystal cathode materials to both improve upon their design and performance or to repurpose them as catalyst supports. This work provides new insights and can inform future studies in the field of transition metal oxide intercalation materials.

Appendix A

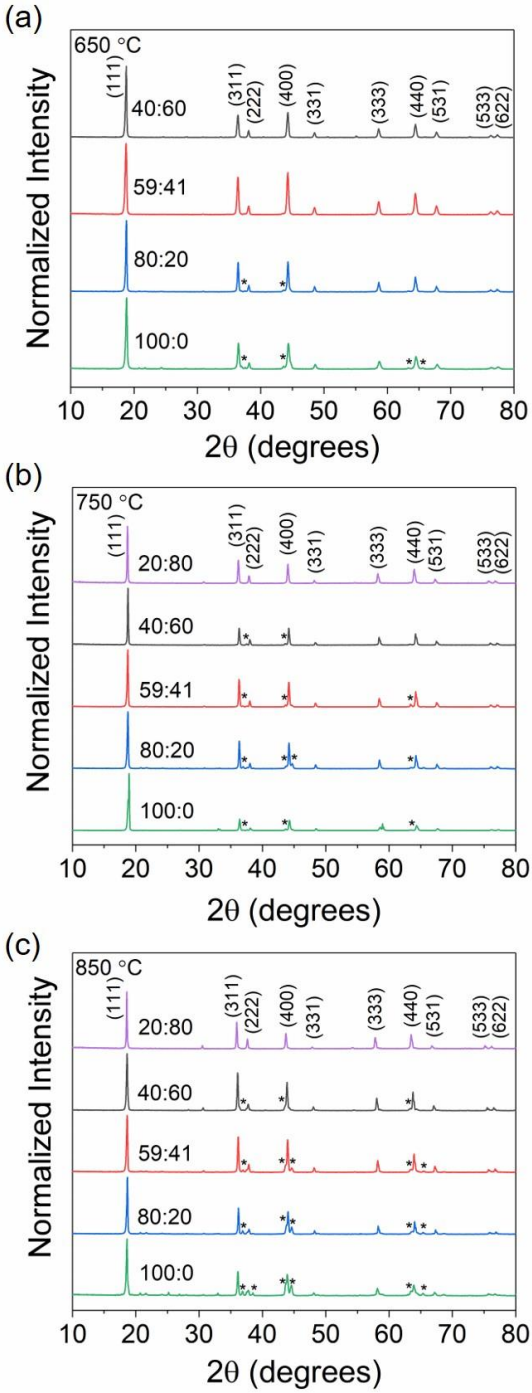

Figure A-1. XRD patterns of LNMO prepared with various LiCl-KCl compositions at (a) 650, (b) 750, and (c) 850 °C. Fd$\bar{3}$m Miller indices are labeled. Asterisks indicate peak locations of rock-salt impurities.

Table A-1. Structural Information Obtained from the Rietveld Refinement Analysis.

Sample	Lattice parameter (Fd3m)	Fractional coordinates			Occupancies	Agreement factors			
(% LiCl_temp)	a (Å)	Mn/Ni x,y,z (16d)	Li x,y,z (8a)	O1 x,y,z (32e)	Mn/Ni (16d)	Rp	Rwp	Rexp	χ^2
100_650	8.152784	0.5	0.125	0.26358	0.06250/0.02083	10.9	14.5	9.15	2.52
80_650	8.164904	0.5	0.125	0.26294	0.05362/0.01812	10.8	14.5	9.57	2.29
59_650	8.158153	0.5	0.125	0.2626	0.06250/0.02083	8.13	10.9	7.09	2.34
40_650	8.162346	0.5	0.125	0.26478	0.06750/0.02250	9.93	13.8	9.70	2.01
100_750	8.194393	0.5	0.125	0.26648	0.06250/0.02083	26.5	34.7	8.24	17.8
80_750	8.19266	0.5	0.125	0.26292	0.06250/0.02083	15.8	21.8	9.67	5.09
59_750	8.186168	0.5	0.125	0.26276	0.06250/0.02083	12.4	17.5	9.46	3.41
40_750	8.197619	0.5	0.125	0.26863	0.06250/0.02083	11.9	16.3	14.00	1.35
20_750	8.224479	0.5	0.125	0.26892	0.06250/0.02083	10.1	13.6	14.20	0.908
100_850	8.222448	0.5	0.125	0.26368	0.06250/0.02083	18.4	26.1	10.10	6.75
80_850	8.207912	0.5	0.125	0.26317	0.06250/0.02083	19.7	27.0	9.66	7.81
59_850	8.216735	0.5	0.125	0.26235	0.06250/0.02083	21.3	31.6	10.00	9.93
40_850	8.242604	0.5	0.125	0.26407	0.06250/0.02083	11.5	15.7	9.41	2.79
20_850	8.281703	0.5	0.125	0.27372	0.06250/0.02083	11.1	14.4	14.20	1.03
59_450	8.162747	0.5	0.125	0.26143	0.06250/0.02083	20.9	32.5	9.13	12.7
59_550	8.161065	0.5	0.125	0.26295	0.06250/0.02083	12.8	19.9	9.60	4.28

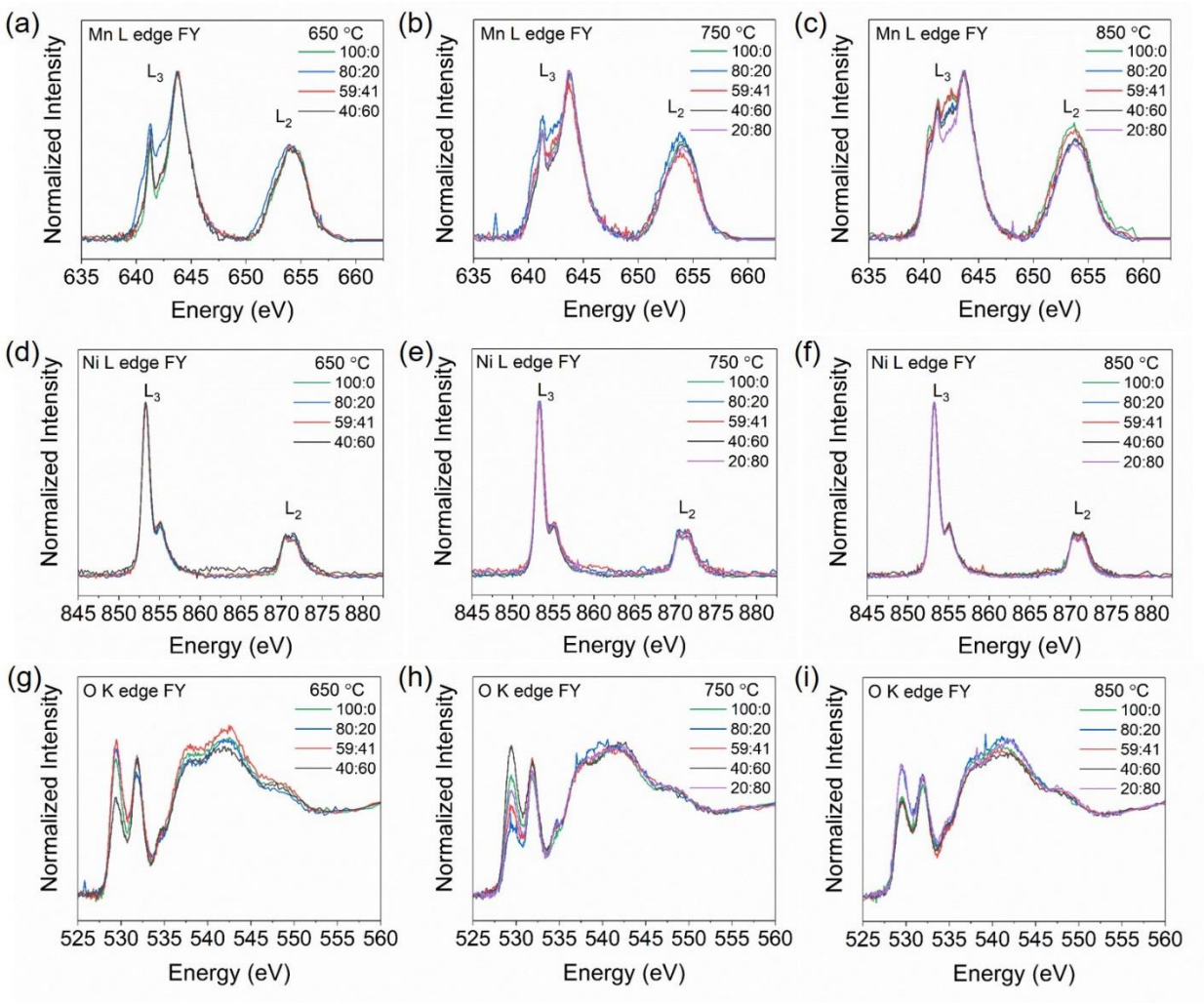

Figure A-2. Soft XAS spectra of LNMO prepared with various LiCl-KCl compositions at (a) 650, (b) 750, and (c) 850 °C in the FY collection mode. (a-c) Mn L-edges illustrating Mn reduction at higher synthesis temperatures and variation of the Mn oxidation state with various salt ratios at fixed synthesis temperatures. (d-f) Ni L-edges illustrating constant oxidation state, and (g-i) O K-edges illustrating decreased TM-O hybridization at higher synthesis temperatures and variation of the TM-O hybridization with various salt ratios at fixed synthesis temperatures.

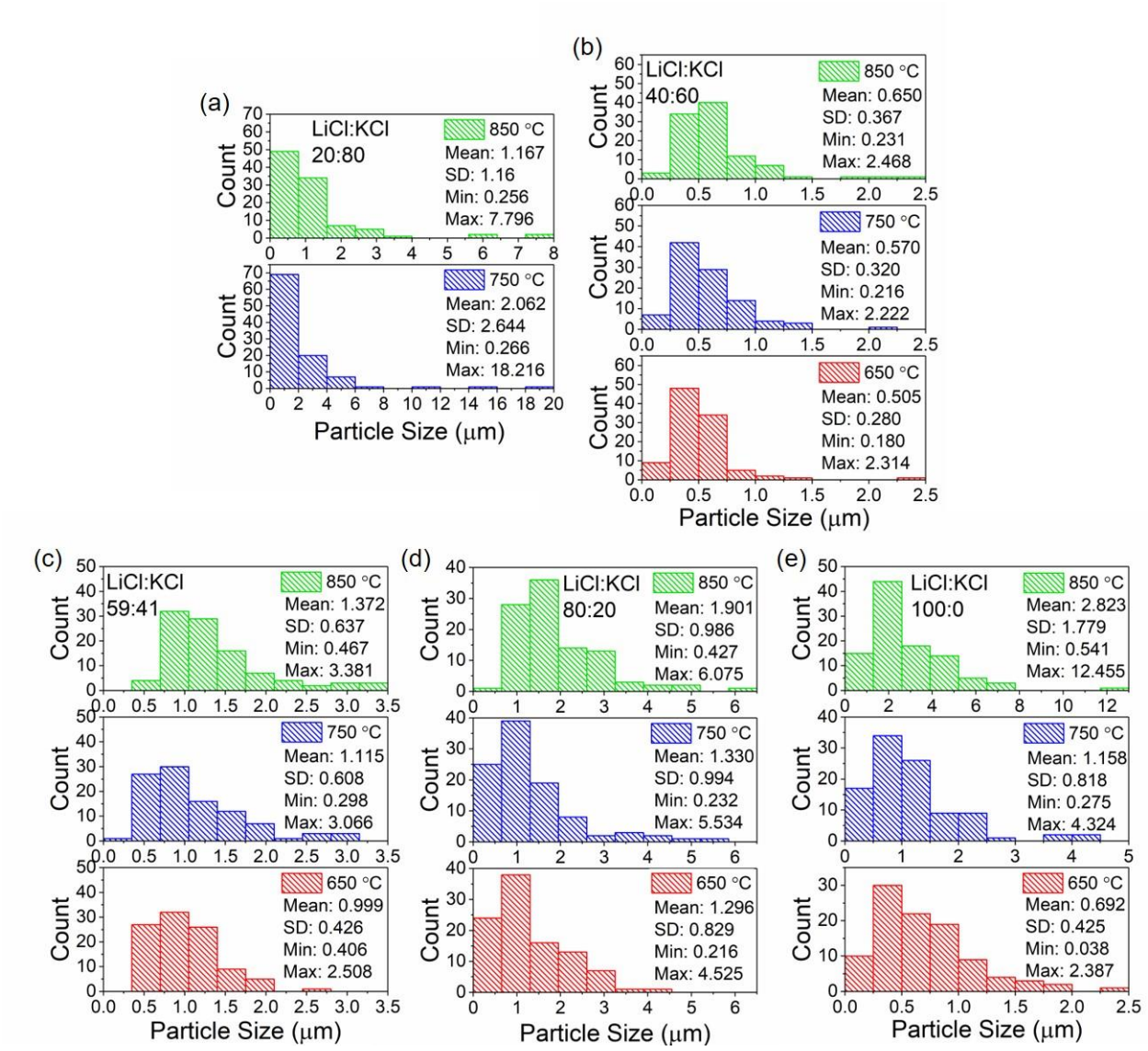

Figure A-3. Size distribution histograms based on SEM images of LNMO prepared with (a) 20:80, (b) 40:60, (c) 59:41, (d) 80:20, and (e) 100:0 LiCl-KCl compositions at 650, 750, and 850 °C.

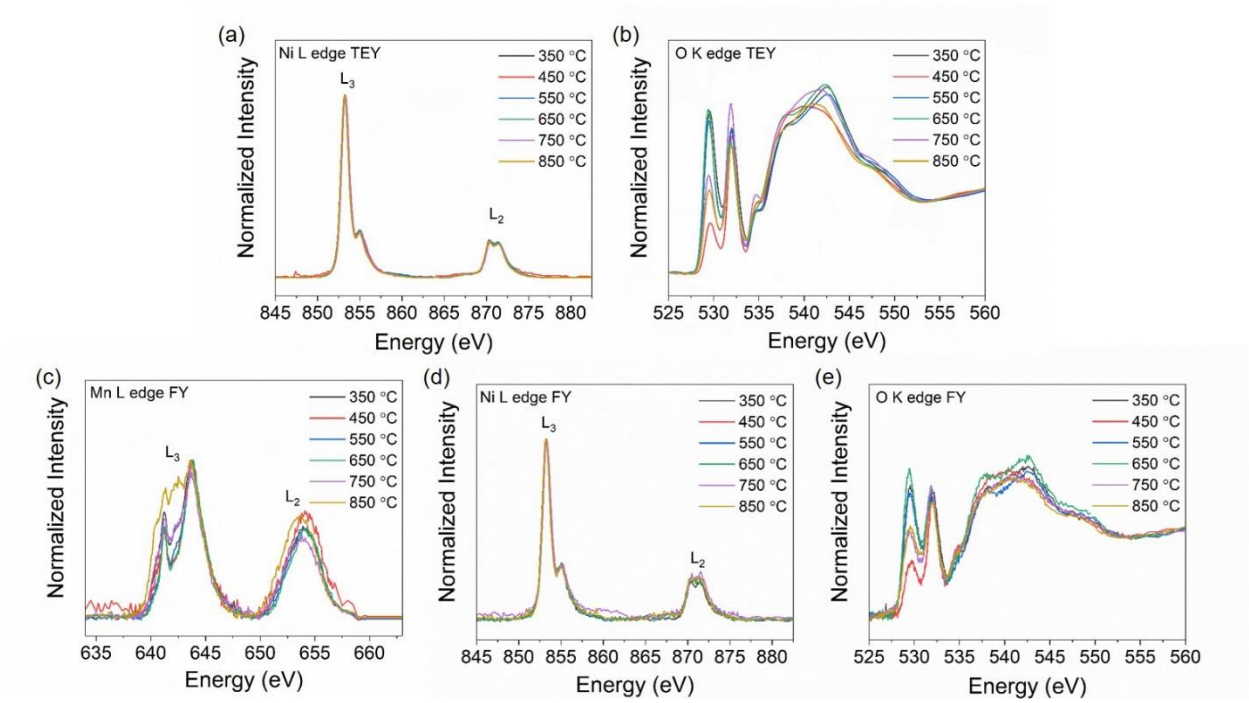

Figure A-4. (a) Ni L-edge XAS spectra and (b) O K-edge spectra in the TEY collection mode. (c) Mn L-edge spectra, (d) Ni L-edge spectra, and (e) O-K edge spectra in the FY collection mode for LNMO samples prepared using eutectic LiCl-KCl at various temperatures.

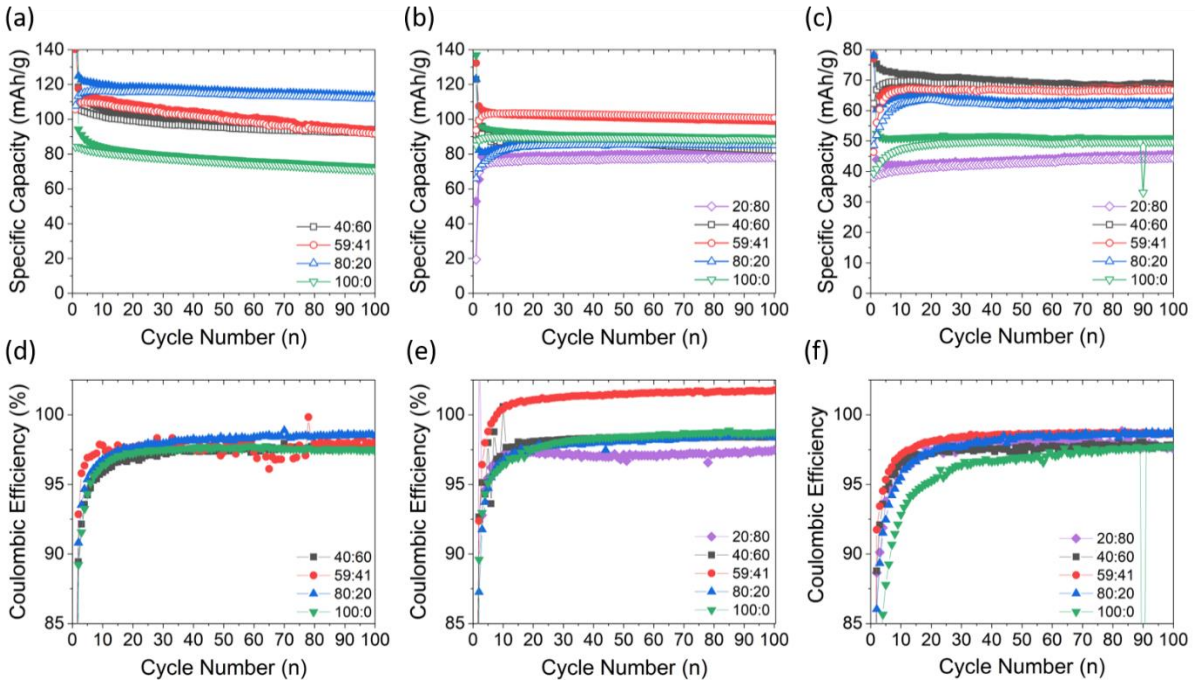

Figure A-9. Cycling performance of LNMO prepared with different LiCl-KCl compositions at (a) 650, (b) 750, and (c) 850 °C between 3.5 and 4.9 V at 0.1 C. Solid symbols represent charge and hollow symbols represent discharge. Coulombic efficiency of LNMO prepared with different LiCl-KCl compositions at (d) 650, (e) 750, and (f) 850 °C. The ratios in the figure represent the molar ratio LiCl:KCl. The measurements were performed at 22 °C.